AGU PUBLICATIONS

Geochemistry, Geophysics, Geosystems

RESEARCH ARTICLE

10.1002/2015GC005751

Provenance of plumes in global convection models

Rakib Hassan[1], Nicolas Flament[1], Michael Gurnis[2], Dan J. Bower[2,3], and Dietmar Müller[1]

[1]EarthByte Group, School of Geosciences, University of Sydney, Sydney, New South Wales, Australia, [2]Seismological Laboratory, California Institute of Technology, Pasadena, California, USA, [3]Now at Department of Earth Sciences, Institute of Geophysics, ETH Zürich, Zürich, Switzerland

Key Points:
- Model plume eruptions are spatially correlated with reconstructed LIPs
- Models with a chemically anomalous deep lower mantle yield better correlations
- Plumes are anchored to deep thermochemical structures that resemble LLSVPs

Correspondence to:
R. Hassan,
rakib.hassan@sydney.edu.au

Citation:
Hassan, R., N. Flament, M. Gurnis, D. J. Bower, and D. Müller (2015), Provenance of plumes in global convection models, *Geochem. Geophys. Geosyst.*, *16*, 1465–1489, doi:10.1002/2015GC005751.

Received 27 JAN 2015
Accepted 17 APR 2015
Accepted article online 24 APR 2015
Published online 26 MAY 2015

Abstract In global convection models constrained by plume motions and subduction history over the last 230 Myr, plumes emerge preferentially from the edges of thermochemical structures that resemble present-day large low shear velocity provinces (LLSVPs) beneath Africa and the Pacific Ocean. It has been argued that large igneous provinces (LIPs) erupting since 200 Ma may originate from plumes that emerged from the edges of the LLSVPs and numerical models have been devised to validate this hypothesis. Although qualitative assessments that are broadly in agreement with this hypothesis have been derived from numerical models, a quantitative assessment has been lacking. We present a novel plume detection scheme and derive Monte Carlo-based statistical correlations of model plume eruption sites and reconstructed LIP eruption sites. We show that models with a chemically anomalous lower mantle are highly correlated to reconstructed LIP eruption sites, whereas the confidence level obtained for a model with purely thermal plumes falls just short of 95%. A network of embayments separated by steep ridges form in the deep lower mantle in models with a chemically anomalous lower mantle. Plumes become anchored to the peaks of the chemical ridges and the network of ridges acts as a floating anchor, adjusting to slab push forces through time. The network of ridges imposes a characteristic separation between conduits that can extend into the interior of the thermochemical structures. This may explain the observed clustering of reconstructed LIP eruption sites that mostly but not exclusively occur around the present-day LLSVPs.

1. Introduction

Mantle plumes of deep origin are invoked to explain time-progressive intraplate volcanism and the appearance of LIPs over short intervals, phenomena that cannot be explained through plate tectonics [*Morgan*, 1971] alone. According to the classical theory of thermal plumes, a rising mantle plume is characterized by a mushroom-like head, atop a narrow conduit, which delivers buoyant material to the rising head [*Richards et al.*, 1989; *Campbell and Griffiths*, 1990; *Campbell*, 2007]. LIP eruptions, with their large volume of melt, putatively result from the arrival of a plume head beneath the lithosphere. Following the eruption of a plume head, long-lived plume tails are thought to be responsible for the continued magmatism associated with hotspot tracks that trail LIPs as they move away from their eruption locations due to plate motions [*Coffin and Eldholm*, 1994; *Ernst and Buchan*, 2002].

Seismic tomographic inversions show the presence of two LLSVPs, below Africa and the Pacific [*Su and Dziewonski*, 1997; *Masters et al.*, 2000; *Ishii and Tromp*, 1999]. The LLSVPs are characterized by seismically observed sharp edges [*Ni et al.*, 2002] and an anticorrelation between bulk sound velocity and shear wave velocity anomalies [*Masters et al.*, 2000] that can be explained by a different chemical composition relative to the ambient mantle. LLSVPs cover about 20% of the core-mantle boundary (CMB) and the mass distribution of the LLSVPs derived from seismic studies is likely responsible for the degree-two geoid anomaly [*Richards et al.*, 1988; *Hager et al.*, 1985]. Laboratory and numerical models have been used to study the dynamics of a dense layer in a convective system [*Gurnis*, 1986; *Christensen and Hofmann*, 1994; *Jellinek and Manga*, 2002; *Davaille et al.*, 2002; *Tackley*, 1998; *Montague and Kellogg*, 2000; *McNamara and Zhong*, 2004]. These studies have shown that the dense layer gets swept toward regions of upwelling in the lower thermal boundary layer (TBL) and subsequently becomes entrained. Earlier studies have also shown that the long-term survival of the dense layer requires a positive density contrast in the range 1%–6% compared to the ambient mantle [*Gurnis*, 1986; *Sleep*, 1988; *Tackley*, 1998; *Gonnermann et al.*, 2002; *Samuel and Farnetani*, 2003; *Zhong and Hager*, 2003; *Tan and Gurnis*, 2005].

Burke et al. [2008] have argued that since no descending slabs have penetrated the LLSVPs and that no LIP-generating plumes have emerged from the interior of these structures, they have remained unchanged for the last 300 Myr. However, results from laboratory and numerical models [*Jellinek and Manga*, 2002; *Davaille et al*., 2002; *McNamara and Zhong*, 2005; *Tan et al*., 2011; *Bower et al*., 2013] suggest that the LLSVPs are susceptible to both entrainment and deformation. Subduction history plays a first-order role in shaping the geometry and location of the LLSVPs [*McNamara and Zhong*, 2005; *Bower et al*., 2013]. Where a plume becomes "anchored" to a dense layer depends on the rheological layering above the CMB [*Davaille et al*., 2002] as the relief of the dense layer must be comparable to, or greater than, the thickness of the thermal boundary layer in order for plumes to become anchored to the dense layer [*Jellinek and Manga*, 2002].

The dense layer acts as a "floating anchor," however, as opposed to a fixed anchor, since the dense layer is displaced by subduction-induced large-scale flow [*Davaille et al*., 2005], which may explain observed inter-hotspot motion [*Davaille et al*., 2002]. Models of thermochemical convection also show that the dense layer morphs into a network of circular embayments separated by sharp ridges [*Tackley*, 1998; *Jellinek and Manga*, 2002; *Deschamps and Tackley*, 2008] and that the base of plumes become pinned to the ridge peaks. *Jellinek and Manga* [2002] showed that the wavelength of the first Rayleigh-Taylor instability in the lower TBL governs the spacing between the centers of these embayments. It is therefore conceivable that the clustering of LIP eruption sites around the present-day LLSVPs [*Torsvik et al*., 2006; *Burke et al*., 2008] can perhaps be explained by the wavelength of initial instabilities pertaining to the TBL above the CMB and the resulting geometry of embayments, which subsequently migrate as a whole to adjust to slab push forces.

Global thermochemical convection models have been formulated and reproduce the pattern of plumes that preferentially emerge from the edges of the LLSVPs [*Tan et al*., 2011; *Steinberger and Torsvik*, 2012]. *Tan et al*. [2011] showed that about half of the strong plumes in models emerge from the edges of thermochemical domes and a qualitative correlation between the location of the strong plumes and the edges of the domes, which move laterally due to large-scale subduction-induced flow. *Steinberger and Torsvik* [2012] presented models where plumes emerge almost entirely from the edges of the LLSVPs, which initially move rapidly in response to subduction-driven flow. *Steinberger and Torsvik* [2012] also report a qualitative assessment that their model plume eruptions, in most cases, can be associated with a LIP eruption site and that their model plumes tend to migrate toward centers of the LLSVPs, compared to corresponding LIP eruption sites.

However, *Austermann et al*. [2014] performed Monte Carlo-based statistical tests to show that reconstructed LIP eruption locations are spatially correlated with both LLSVPs and the edges of these structures. Since these correlations were statistically indistinguishable, they argued that conclusions derived from global thermochemical convection models [*Tan et al*., 2011; *Steinberger and Torsvik*, 2012] may not be robust. *Davies et al*. [2015] showed, based on statistical analyses, that reconstructed LIPs and hotspots in the Indo-Atlantic domain are spatially correlated with the edges of the African LLSVP—however, reconstructed LIPs and hotspots in the Pacific domain fail to show any spatial correlation with the Pacific LLSVP. Although it should be noted that the western two-thirds of the area in the Pacific vertically above the underlying LLSVP is devoid of any reconstructed LIPs (Figure 3b). This is likely due to subduction of LIPs that were once further to the west of the Shatsky Rise—see *Torsvik et al*. [2006] for a more detailed discussion. A statistical analysis of the spatial distribution of model plume eruptions can offer insights precluded by the limited reconstructed LIP sites in the Pacific domain.

In global convection models with assimilation of plate tectonic evolution over the last 230 Myr, we analyze the displacement and deformation of a dense layer and show that the resulting shapes are similar to LLSVPs, with plumes at their edges. We present a statistical analysis of the model plume eruption sites and their correlation with reconstructed LIP eruptions. We also investigate the effect of the initial thickness and intrinsic density contrast of the dense layer on the evolution of its geometry by entrainment and subduction-driven large-scale flow. We observe slab descent rates and plume-related observables in models, particularly the temperature differential between plume material and the ambient upper mantle and plume buoyancy fluxes derived from it, to assess the robustness of models. The models allow us to consider alternative scenarios that might explain the clustering of reconstructed LIP eruption sites in the last 200 Myr.

Table 1. Physical Parameters and Constants

Parameter	Symbol	Value	Units
Rayleigh number	Ra	5×10^{8}	
Earth radius	R_0	6371	km
Density	ρ_0	3930	kg m^{-3}
Thermal expansivity	α_0	1.42×10^{-5}	K^{-1}
Thermal diffusivity	κ_0	1×10^{-6}	m^2 s^{-1}
Specific heat capacity	C_p	1100	J kg^{-1} K^{-1}
Gravitational acceleration	g	10	m s^{-2}
Surface temperature	T_s	300	K
Dissipation number	Di	0.8	
Reference viscosity	η_0	1×10^{21}	Pa s
Internal heating	H	100	

2. Methods

2.1. Governing Equations

We consider thermochemical models of the Earth's mantle under the extended-Boussinesq approximation [*Christensen and Yuen*, 1985; *Ita and King*, 1994; *Zhong*, 2006] in a spherical shell. The equations for the conservation of mass, momentum, and energy are cast as a finite element problem and solved using CitcomS [*Zhong et al*., 2000, 2008], which has been modified to allow for progressive assimilation of surface plate motion and inferred slab material based on global plate reconstructions [*Bower et al*., 2015].

The equation for mass conservation in incompressible flow is

$$\nabla \cdot u = 0, \tag{1}$$

where u is the velocity vector. The nondimensional momentum equation is

$$-\nabla P + \nabla \cdot \tau = (CB - \alpha T) g Ra e_r, \tag{2}$$

where P, τ, C, B, α, T, Ra, g, and e_r are the dynamic pressure, deviatoric stress tensor, proportion of compositionally distinct material, the ratio of chemical density anomaly to the maximum thermal density anomaly in the system, coefficient of thermal expansion, temperature, Rayleigh number, acceleration due to gravity, and radial unit vector, respectively. B is defined as

$$B = \frac{\Delta\rho_{ch}}{\rho_0 \alpha_0 \Delta T}, \tag{3}$$

where $\Delta\rho_{ch}$, ρ_0, and ΔT are the chemical density anomaly, density, and the total temperature drop across the mantle, respectively. Quantities subscripted with "0" represent dimensional reference values. The Rayleigh number is defined as

$$Ra = \frac{\rho_0 \alpha_0 \Delta T {R_0}^3 g_0}{\eta_0 \kappa_0}, \tag{4}$$

where R_0, η_0, and κ_0 are the radius of the Earth, viscosity, and thermal diffusivity, respectively. Using the radius of the Earth instead of the thickness of the mantle scales Ra by a factor of ≈ 11, compared to that derived from the usual definition.

The nondimensional energy equation is

$$c_p \frac{\partial T}{\partial t} = -c_p u \cdot \nabla T + \nabla \cdot (c_p \kappa \nabla T) - Di(T + T_s)\alpha g u_r + \frac{Di}{Ra}\tau : \dot{\epsilon} + H, \tag{5}$$

where c_p, Di, T_s, $\dot{\epsilon}$, and H are the heat capacity at constant pressure, dissipation number, surface temperature, strain rate tensor, and internal heating rate, respectively. The dissipation number, Di, is defined as

$$Di = \frac{\alpha_0 g R_0}{c_p}. \tag{6}$$

Parameters held fixed across all model cases are listed in (Table 1). Chemical advection is governed by

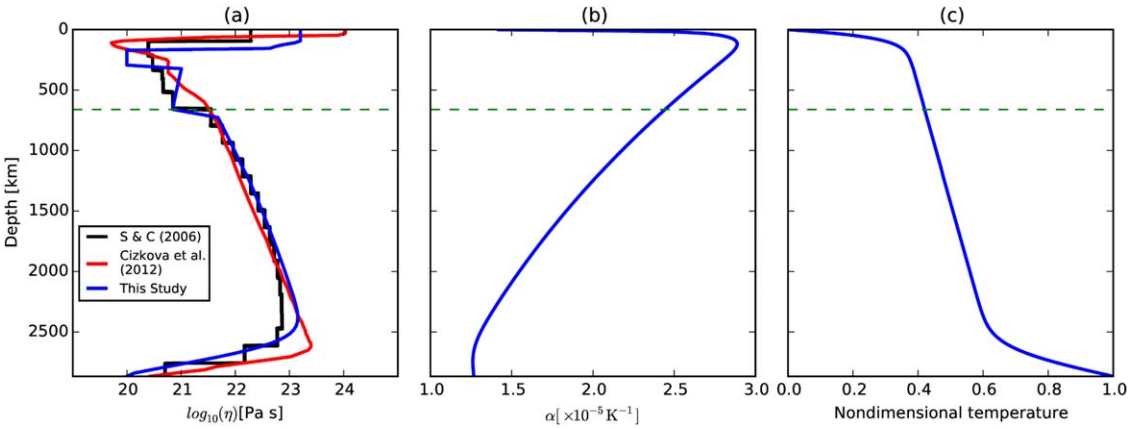

Figure 1. (a) Viscosity, (b) thermal expansivity, and (c) initial mantle temperature.

$$\frac{\partial C}{\partial t}+(u\cdot\nabla)C=0. \tag{7}$$

Composition is advected using tracer particles [*McNamara and Zhong*, 2004]. The trajectory of a tracer particle is computed using a predictor-corrector scheme and the composition, C, is computed using the ratio method [*Tackley and King*, 2003]. In the ratio method, the anomalous composition at a spatial location is the ratio of the anomalous tracers to the total number of tracers in the neighborhood. Since the advection of tracers is computationally expensive [*McNamara and Zhong*, 2004], we limit the number of tracers in our models to about 30 tracers per element initially, similar to *Zhong et al*. [2008]. We further reduce the computational cost of advecting tracers by removing ambient tracers between 410 and 2600 km depths and impose $C = 0$ in elements that contain no tracers.

2.2. Model Setup

The full spherical shell is composed of 12 parts, each subdivided into 128 × 128 × 64 elements, amounting to a total of ≈12.6 million elements. The mesh is refined radially to provide a vertical resolution of ≈15 km and ≈27 km near the top and bottom boundary layers, respectively. The minimum radial resolution in the midmantle is ≈109 km. The lateral resolution is ≈50 km and ≈28 km at the surface and the CMB, respectively.

We compute a reference profile for thermal expansion based on analytical parameterizations of $\alpha(T,z)$ given in *Tosi et al*. [2013] equation (2):

$$\alpha(T,z)=(b_0+b_1T+b_2T^{-2})exp(-b_3z), \tag{8}$$

where T and z are the absolute temperature and depth, respectively. The coefficients b_0, b_1, b_2, and b_3 are obtained from the inversion of thermodynamic data obtained from first-principles simulations, followed by the numerical integration of the PREM density and gravity profile [*Tosi et al*., 2013]. We assume an a priori mantle adiabat augmented by TBLs. The top and the bottom TBLs each encompass a temperature drop of 1225 K and the initial adiabatic temperature profile has a potential temperature of 1525 K. We use this a priori mantle temperature profile to compute our reference thermal expansion profile (Figure 1).

We compute the reference density profile by numerically integrating a parameterization of $\rho(r)$ [*Solheim and Peltier*, 1990]:

$$\rho(r)=exp\left(-\int_{r_{sur}}^{r}\frac{Di}{\gamma}\frac{dr}{d}\right), \tag{9}$$

where γ, r, and d are the Grüneisen parameter, radius, and the depth scale of the mantle, respectively. We use an a priori analytical form of $\frac{Di}{\gamma}$, equation (37) in *Solheim and Peltier* [1990], derived based on the lower mantle PREM density data.

We use piecewise Arrhenius laws to describe the variation of viscosity with temperature, depth, and composition in the upper and lower mantle, which takes the following nondimensional form:

$$\eta(T,r)=A(r)\eta_c exp\left(\frac{E_a(r)+(1-r)V_a(r)}{T+T_{off}}-\frac{E_a(r)+(1-r_{inner})V_a(r)}{1+T_{off}}\right), \quad (10)$$

where r, A, η_c, E_a, V_a, and T_{off} are the radius, preexponential parameter, intrinsic composition-dependent prefactor, activation energy, activation volume, and temperature offset, respectively. The second term within the exponential ensures that it reduces to 1, where $T=1$ and $r=r_{inner}$. We only apply the composition-dependent prefactor to compositionally distinct continental lithosphere [see *Flament et al*., 2014]. For the lower mantle, we use a dimensional activation energy of 320 kJ/mol and activation volume of 6.7E-6 m^3/mol, corresponding to nondimensional units of 11 and 26, respectively, comparable to estimates in *Karato and Wu* [1993]. However, such viscosity parameterizations lead to large viscosity variations, causing numerical difficulties. In order to limit the viscosity contrast to a factor of ≈1400, we adjust the preexponential parameter $A(r)$ and the temperature offset T_{off} [*Tackley*, 1996]. The resulting viscosity profile (Figure 1a) is similar to the preferred viscosity profiles of *Steinberger and Calderwood* [2006] and that in *Čížková et al*. [2012].

A nondimensional internal heat generation rate of 100 is applied in all test cases, which is similar to that used in earlier studies [e.g., *Bunge*, 2005; *Zhong*, 2006; *Leng and Zhong*, 2008; *Zhang et al*., 2010]. The petrological estimates of plume excess temperature (difference in temperature between plumes and ambient mantle) range between 200 and 300 K [*Schilling*, 1991], which is low compared to the temperature drop across the lower TBL. *Bunge* [2005] showed that plume excess temperature systematically decreases from the CMB toward the top TBL, well within petrologic estimates, due to adiabatic cooling on the one hand and the subadiabaticity of the mantle geotherm resulting from internal heating on the other hand. These conclusions were further reinforced in subsequent studies [*Zhong*, 2006; *Leng and Zhong*, 2008].

At the CMB, we apply an isothermal ($T=1$) and free-slip boundary condition, while at the surface we impose an isothermal ($T=0$) and kinematic boundary condition. The combination of large velocity gradients and high viscosities in the upper thermal boundary layer (TBL), resulting from the temperature-dependent viscosity, produces intense localized heating at plate margins. This leads to large gradients in strain rate and viscosity which may cause numerical difficulties [*Bower et al*., 2013]. Consequently, following *Bower et al*. [2013], we set the dissipation number, Di, to zero for depths shallower than 320 km.

2.3. Progressive Data Assimilation

We impose kinematic boundary conditions, derived from global plate tectonic reconstructions modified from *Seton et al*. [2012], in 1 million year intervals and a linear interpolation in between. The global reconstructions are based on a moving hotspot reference frame [*Torsvik et al*., 2008] for the last 70 Ma and a True Polar Wander (TPW)-corrected paleomagnetic reference frame [*Steinberger and Torsvik*, 2008] for earlier ages. Plate velocities are extracted from these reconstructions with continuously closing plates [*Gurnis et al*., 2012] and exported using GPlates [*Boyden et al*., 2011].

In addition to the kinematic boundary conditions, we assimilate the thermal history of the lithosphere and shallow slabs. Following *Flament et al*. [2014], we use a half-space cooling model to derive a global temperature field of the lithosphere based on the global plate reconstruction in the oceans, and on tectonothermal ages [*Artemieva*, 2006] in the continents. A thermal model of slabs is constructed based on the reconstructed location and age of oceanic lithosphere at convergent plate margins (Figure 2a). A slab dip angle of 45° is applied for depths shallower than 350 km and a half-space cooling model is used to construct the thermal profile on either side of the slab centerline, in order to conserve buoyancy. These slabs are initially inserted from the surface to a depth of 1200 km. Slabs that appear during modeled geological time are progressively inserted into the upper mantle based on their age of appearance. This imposed thermal structure is blended with the dynamically evolving temperature field at each time step—see *Bower et al*. [2013, 2015] for a more detailed description of the progressive data assimilation method. This approach captures the essential aspects of subduction—which injects slabs with realistic thickness and mass flux—despite the lack of complex rheological laws and the requisite resolution necessary to model the physics of plate boundaries in our models.

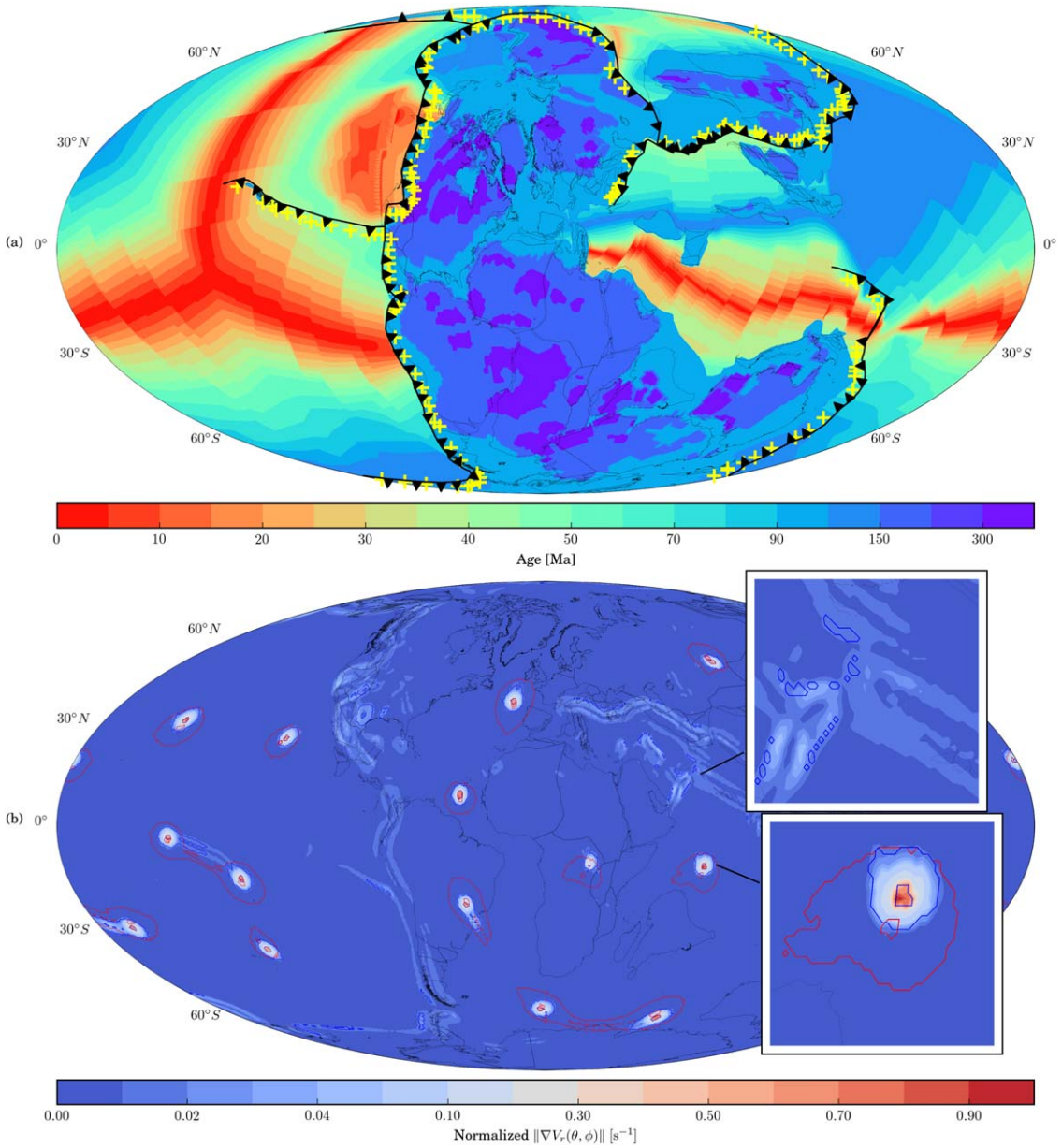

Figure 2. (a) Age of lithosphere and plate reconstruction at 230 Ma. The yellow "plus" symbols represent tracer particles placed at 200 km depth that we use to track the descent of slab material. See text for more details. (b) Normalized magnitude of spatial gradient of the radial velocity vector at 350 km depth and reconstructed coastlines, both at 85 Ma. Blue contours show result of *k*–means clustering at 350 km depth and that of red at 1500 km depth.

2.4. Slab Descent Rate

We track the descent rate of slabs using a fourth order Runge-Kutta scheme as a postprocessing step with tracer particles emplaced at a depth of 200 km along subduction boundaries (Figure 2a) and subsequently tracked in the evolving flow field from the beginning to the end of model time. We compare the computed slab descent rates to estimates from *Van der Meer et al*. [2009] and this serves as an important diagnostic for the evolution of our convection models.

2.5. Plume Detection Scheme

Plume detection schemes that rely on their anomalous temperature have been outlined in earlier work [*Labrosse*, 2002; *Zhong*, 2005, 2006; *Boschi et al*., 2007; *Leng and Zhong*, 2008; *Leng and Gurnis*, 2012]. *Labrosse* [2002] used an image analysis procedure of finding connected components in a three-dimensional

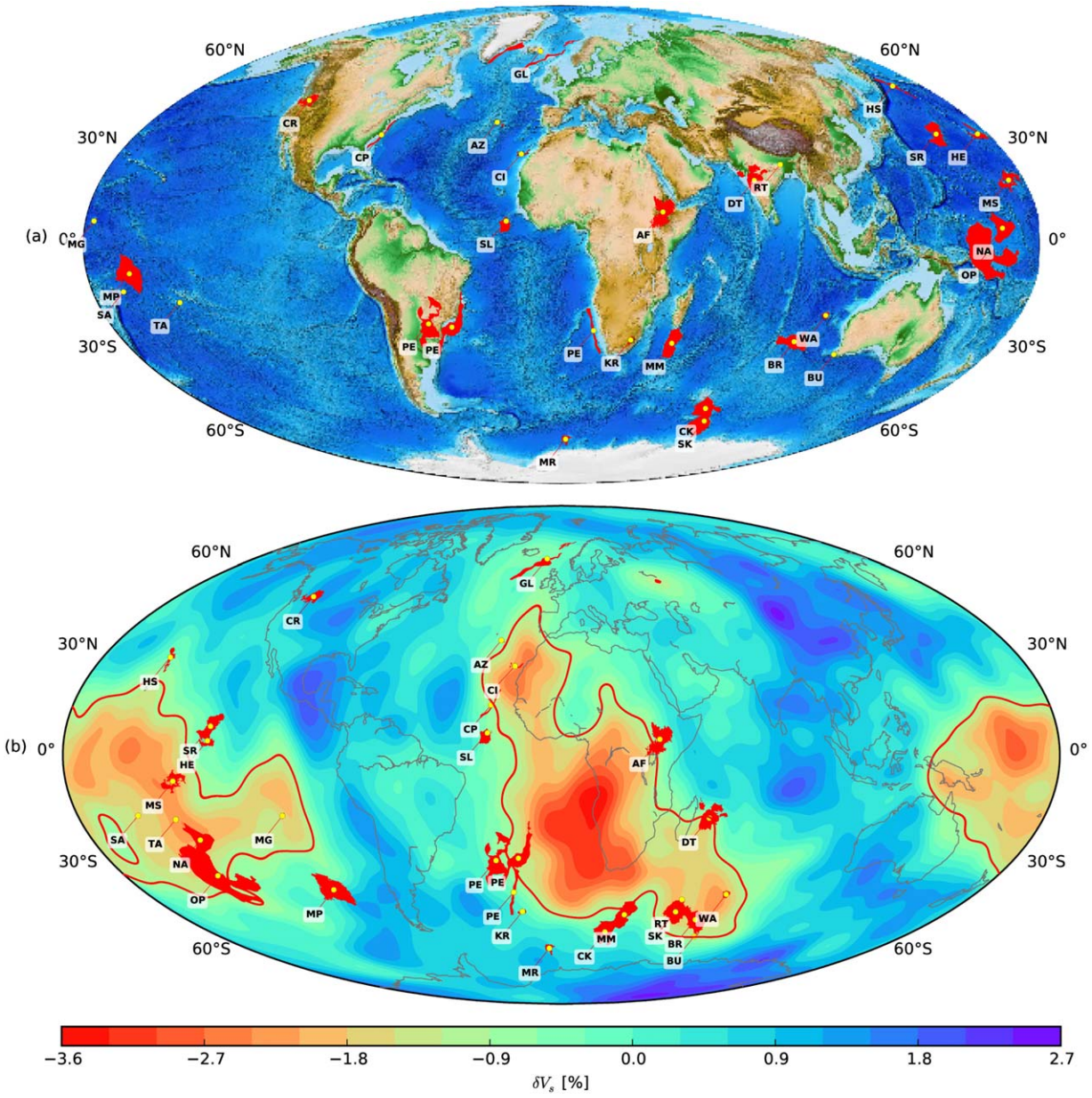

Figure 3. (a) Present-day locations of LIPs (red regions) and hotspots, sourced from plumes of deep origin—see in text for more details. ETOPO global relief is shown in the background, with the centroids of LIPs and hotspots represented by yellow circles. (b) Reconstructed locations of these surface features in Figure 3a. SMEAN tomography at depth 2850 km, expressed as percentage V_s wave speed variation relative to PREM—with layer average removed—is shown in the background. The −1% contour is shown in red.

temperature field based on a threshold value. *Zhong* [2006] outlines a similar plume detection algorithm where the temperature field is scanned at a given time step and radius r, to find the maximum temperature T_{max}. He also computes the horizontally averaged temperature, $T_{bg}(r)$, for each radial shell excluding cold downwellings. The temperature field is then iteratively scanned to identify the location (θ_i, ϕ_i) with the highest temperature T_i and if $T_i > \{T_{bg}(r)+f(T_{max}-T_{bg}(r))\}$—where f is a factor between 0 and 1—it is counted as a plume and excluded from subsequent scans. For each of these identified plumes, neighboring locations within an arc distance of r_{arc} are attributed to these plumes if their radial velocities are positive and their temperature is greater than $T_{bg}(r)$—these neighboring locations are also excluded from subsequent scans of the temperature field. A similar approach is used to detect plumes in a high-resolution study of plume observables in *Leng and Zhong* [2008] and *Leng and Gurnis* [2012]. Another alternative form of this procedure is outlined by *Boschi et al.* [2007], where in addition to identifying the extent of a plume at a

given depth, the neighboring volume is also scanned—similar to *Labrosse* [2002] finding connected components—to identify vertically contiguous structures, allowing large plume tilts.

However, these procedures suffer from the limitation that the choice of the threshold value results in discounting legitimate plumes, or breaking them in part, if too high. On the other hand, shallow temperature anomalies not related to plumes—such as in the mantle wedge around subduction zones—are counted as plumes if the threshold value is too low. Furthermore, the time-dependent nature of plume flux, from eruption to their subsequent waning, the distortion of plume conduits under fast moving plates, their spatial variability in 3-D global spherical models, and their variance between different models bring additional challenges to the process of automatically identifying plumes in a reliable manner. A robust plume identification scheme must therefore be able to cope with the space-time variability of plume evolution.

We use a new plume detection scheme based on a *k*–means clustering algorithm [*Lloyd*, 1982]. Such algorithms partition items into *k* clusters such that the sum of the distances over the items in each cluster to their cluster center is minimal, i.e., given a set of observations $(x_1, x_2, ..., x_n)$, where each observation can be *d* dimensional, *k*–means clustering partitions the *n* observations into $k(\leq n)$ sets $S=\{S_1, S_2, ..., S_k\}$ by minimizing the objective function:

$$\underset{x}{\operatorname{argmin}} \sum_{i=1}^{k} \sum_{x \in S_i} \|x-\mu_i\|^2, \tag{11}$$

where μ_i is the mean of points in set S_i. An efficient heuristic algorithm, e.g., the expectation-maximization algorithm is commonly used to compute the partitioning into *k* groups, where the number of clusters *k* is specified by the user. The algorithm starts by assigning items randomly to clusters and iteratively computes the centroid of each cluster and subsequently reassigns items to the cluster whose centroid is now the closest to them. The iteration stops when no items require reassignment. Optimal clustering is found by repeating the algorithm many times, each time starting from a different initial random clustering.

At a given time and depth, we compute the global spatial gradient of the radial velocity vector, $\nabla V_r(\theta, \phi)$, based on the algorithm in *Renka* [1984], for which the code is publicly available [*Renka*, 1997]. We then compute a histogram of $||\nabla V_r(\theta, \phi)||$ and exclude all values below the 95th percentile and values for which the radial velocities $V_r(\theta, \phi)$ are negative from subsequent processing. We call this subset Ω_n, where the value of subscript *n* denotes depth in km. Ω_n essentially comprises a number of isolated patches, each representing a putative plume conduit. This is a reasonable approach because plume conduits are characterized by large values of $||\nabla V_r(\theta, \phi)||$ and the combined cross sectional area of our model plumes, at any given time, is always $<$2% of the global surface area (Figure 2b).

We then apply *k*–means clustering on Ω_{350} and Ω_{1500}, imposing the number of clusters $k = 2$, which partitions Ω_{350} and Ω_{1500} into clearly defined inner and outer regions in the cases of legitimate plume conduits. However, this does not hold in the cases of shallow temperature anomalies such as in the mantle wedge near subduction zones and is therefore a key criterion for excluding such shallow temperature anomalies from being erroneously counted as plume conduits. We check the continuity of a plume conduit by ensuring that the inner region of a conduit identified in Ω_{350} is mirrored by a corresponding inner region in Ω_{1500}, within a maximum lateral offset of 1000 km. Figure 2b shows the contours of inner and outer regions of Ω_{350} and Ω_{1500}, for a typical model at 85 Ma, in blue and red, respectively. The exclusion of shallow temperature anomalies near subduction zones is clearly seen in the absence of larger red contours mirroring them at a depth of 1500 km. The centers of plume conduits are then located by the maximum radial velocities in the corresponding inner regions of Ω_{350}.

A statistical analysis of model plumes, introduced in the next section, requires a robust scheme for detecting plume eruptions throughout a given model run. Such a robust scheme also allows for quantitatively tracking the excursion of model plume conduits subsequent to their eruption, as seen from their trails projected on an interface near the surface of the Earth. For our purposes, we track model plumes by their trails projected on a surface at a depth of 350 km. The choice of this depth is primarily driven by the necessity to avoid the plume head so as to be able to focus the above analysis on the conduit just below it. We register the eruption of a plume $P_E(\theta_i, \phi_i)$ at 350 km depth—based on the algorithm described above—if a plume has not been detected in a 500 km radius of (θ_i, ϕ_i) in the preceding 5 Myr. This is a reasonable approach

since we process model outputs at 5 Myr intervals, based on the fact that the transit time of our model plumes from the CMB to the base of the lithosphere is >5 Myr. Whenever we refer to model plume eruptions, we refer to this definition, unless stated otherwise.

2.6. Statistical Significance of Model Plumes

Most LIPs of the past 200 Myr reconstructed to their ages of eruption and projected radially downward lie at the edges of LLSVPs [*Burke and Torsvik*, 2004; *Torsvik et al*., 2006; *Burke et al*., 2008]. *Torsvik et al*. [2006] showed that reconstructed LIPs lie within $\pm 10^{\circ}$ of the 1% slow shear wave velocity contour in the SMEAN tomographic model. They further argued that the spatial correlation of LIP eruption sites to the margins of the LLSVPs is robust, given that their application of four different reconstruction methods, namely, Africa fixed hotspot, Africa moving hotspot, global moving hotspot, and global paleomagnetic, produced similar patterns where LIP eruption sites cluster around the 1% slow velocity contour at the CMB.

We take the *Coffin and Eldholm* [1994] compilation of LIPs and exclude all putative LIP sites, except the ones listed in Table 1 of *Torsvik et al*. [2006]. From this subset we further exclude the Siberian Traps, since our convection models only span the last 230 Myr. We also exclude the components of CAMP in North West Africa and Northern South America, primarily due to their coverage compared to other LIPs. We adopt the symbols for these LIP sites from Table 1 of *Torsvik et al*. [2006]. We add six additional surface features thought to be connected to plumes of deep origin [*Steinberger*, 2000], namely, Tahiti (TH), Samoa (SA), Azores (AZ), Canary (CI), Hawaii (HS), and Easter (MS). The present-day location of these sites, which we reconstruct based on a moving hotspot reference frame [*Torsvik et al*., 2008] for the last 70 Ma and a True Polar Wander (TPW)-corrected paleomagnetic reference frame [*Steinberger and Torsvik*, 2008] for earlier ages, is shown in Figure 3a.

The reconstructed locations of these sites—similar to those presented in *Torsvik et al*. [2006]—with SMEAN tomography at a depth of 2850 km in the background, expressed as percentage V_s wave speed variation relative to PREM, with layer average removed is shown in Figure 3b. From here on, we will refer to LIPs at their reconstructed locations, unless stated otherwise.

We apply a Monte Carlo approach, similar to that in *Austermann et al*. [2014], to test for spatial correlation between model plume eruption sites and LIPs. Monte Carlo testing entails ranking the value of u_1 of a test statistic u, from a corresponding set of values generated by drawing random samples from the null distribution of u [*Besag and Diggle*, 1977]. To obtain a proper assessment of the significance of u_1, we carry out $m-1$ simulations based on random sampling of the null distribution of u and compute the corresponding quantities $u_2, \ldots, u_m$. The significance level of u_1 is then simply derived from the position of u_1 when the set $\{u_1, \ldots, u_m\}$ is numerically sorted—see *Besag and Diggle* [1977] for more details.

For our purposes, we proceed from the null hypothesis that model plume eruption sites are not correlated with LIPs. We compute u_1 as the cumulative angular distance between model plume eruption sites and their closest LIPs, represented by their centroids:

$$u_1 = \sum_{i=1}^{N_E} D(P_i, L), \tag{12}$$

where N_E, P_i, L, and D are the total number of plume eruptions detected in a given convection model, spatial location of the i^{th} model plume eruption, set of the centroids of LIPs, and the function that computes the angular distance of a point (P_i) to the closest point in a point-set (L), respectively. D is defined as

$$D(x, L) = \underset{y \leftarrow L}{\operatorname{argmin}}\, D(x, y). \tag{13}$$

We then create $m-1$ ($\approx$50,000) realizations, each containing the spatial locations of N_E plume eruptions randomly placed on the sphere—these random locations are drawn from a distribution that is uniform in space. Subsequently, we compute the quantities $u_2, \ldots, u_m$ just as we compute u_1 and the significance of our model plume eruptions is derived from the position of u_1 in the ordered set $\{u_{(1)}, \ldots, u_{(m)}\}$. In other words, if u_1 is smaller than 95% of the cumulative angular distances obtained from Monte Carlo sampling, i.e., values in the set $\{u_2, \ldots, u_m\}$, model plume eruptions are deemed spatially correlated to LIPs.

Table 2. Model-Specific Parameters and Results[a]

	Input Parameters			Output Parameters		
Case	Δd	B	$\Delta\rho_{ch}$%	N_E	P_0 (Ma)	P_p
M1	0	0	0	19	195	14
M1L[b]	0	0	0	85		21
M2	100	0.25	1.25	27	185	14
M3	100	0.5	2.5	33	175	10
M4	100	0.6	3.0	31	170	15
M5	100	0.7	3.5	26	165	12
M5L[c]		0.7	3.5	69		16
M6	100	1.0	5.0	20	160	13
M7	150	0.6	3.0	24	149	11
M8	150	0.7	3.5	22	145	12
M9	200	0.6	3.0	21	124	11
M10	200	0.7	3.5	21	119	10
M11[d]		0.7	3.5	49		13

[a]Δd, $\Delta\rho_{ch}$, N_E, P_0, and P_p are the thickness of the dense thermochemical layer, its anomalous chemical density as a percentage, total number of plume eruptions throughout the model run, age of eruption of the first plume, and the number of plumes at present-day, respectively. Since the initial condition for models M1L, M5L, and M11 has preexisting plumes, we do not list the age of eruption of the first plume.

[b]Initial condition for this model is derived from a free-slip convection model—see text for more details.

[c]Initial condition and initial topography of the dense thermochemical layer for this model is derived from a free-slip convection model—see text for more details.

[d]Initial topography of the dense thermochemical layer for this model is derived from case M5 at 75 Ma.

3. Results

We present a total of 11 test cases computed from 230 Ma to the present, where we varied the thickness of the initial dense layer above the CMB and the buoyancy ratio, B, keeping all other parameters constant. We also present two additional test cases initiated with an unbiased distribution of plumes. The model parameters for each case, along with key outcomes (total number of plume eruptions, age of the eruption of the first plume, and number of plumes at present-day) are given in Table 2.

3.1. Models with Purely Thermal Plumes

We first describe model M1 with an isochemical lower mantle where the TBL above the CMB thickens in response to the subduction-induced large-scale flow and incipient plumes develop within the first 30 Myr of model time. The development and subsequent eruption of a plume beneath Greenland at 190 Ma is indicative of typical behavior in which the location of the plume nucleation is induced by descending slabs to the east and west (the Tethys and western North America, respectively; Figure 4). Note that the spatial gradients related to subduction zones (Figure 4a) are relatively small compared to that associated with plume conduits; consequently, the subduction feature prominently in the normalized plot prior to eruption of plumes (Figure 4b).

A total of 19 plume eruptions were detected of which most appeared within the first 100 Myr of model time (Figure 5a) and a total of 14 plumes survive to the present-day (Table 2). Plume conduits are rooted on the CMB (Figure 4 right) and the strong temperature dependence of viscosity results in large velocities within the conduits with rather large excess temperatures relative to petrological estimates at a depth of 350 km (Figure 5e). The transit times of these plumes from the CMB to the surface range between 10 and 15 Myr. The plume conduits are long-lived, but their roots migrate laterally to adjust to slab push forces, as shown by trails of plume conduits at a depth of 350 km in relation to the location of subduction zones over the last 230 Myr (Figure 6). Slab sinking rates in the upper mantle are comparable to published estimates [*Van der Meer et al.*, 2009] but are considerably reduced in the deep lower mantle (Figure 5d).

Model M1L, analogous to model M1, but initiated with an unbiased distribution of plumes, is described in more detail in section 3.3.

3.2. Models with Thermochemical Plumes

Models M2–M10 comprise a uniform dense layer of varying thicknesses and buoyancy ratios, B, above the CMB in the initial condition. Model M11, described further on, comprises preexisting plumes in the initial

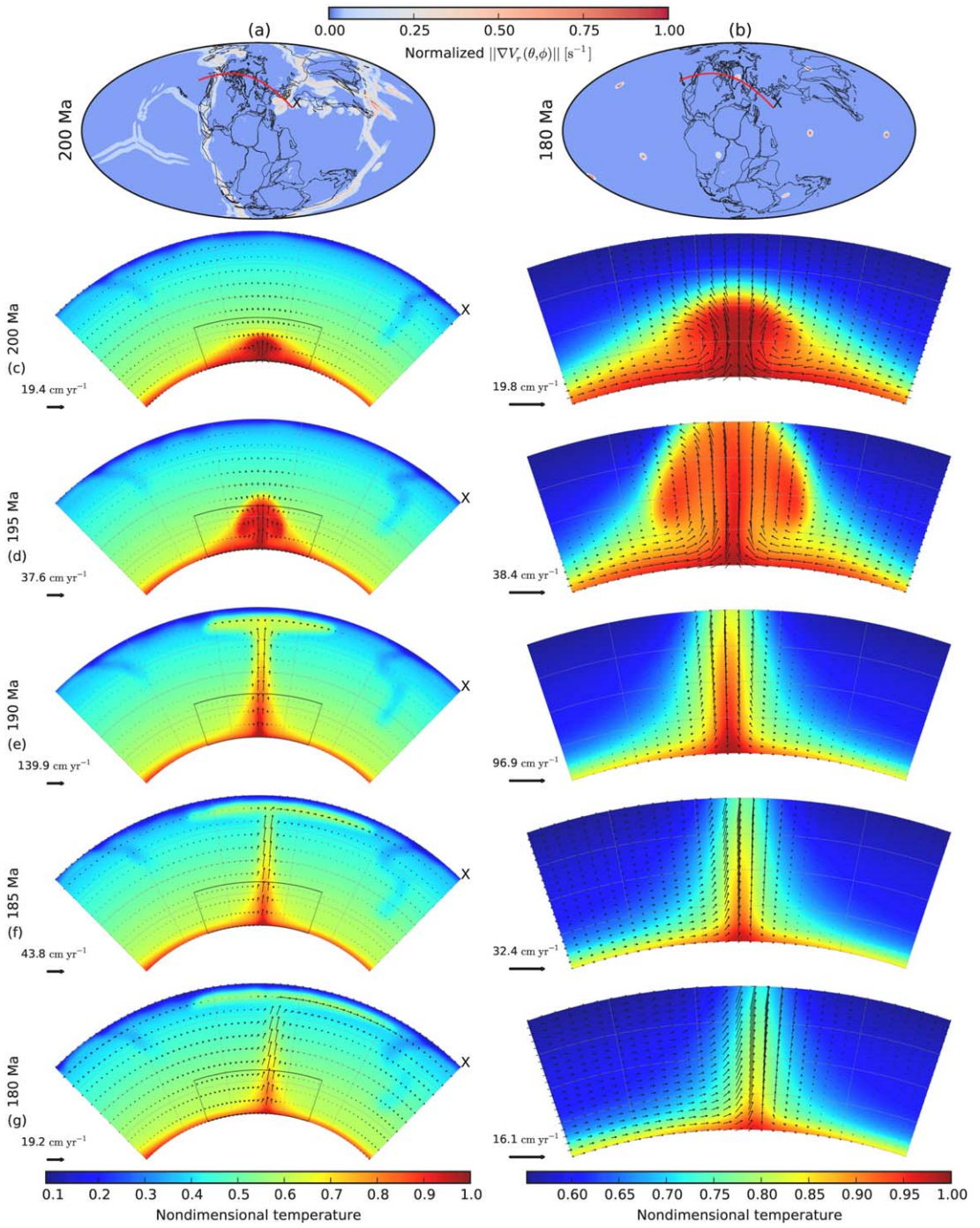

Figure 4. (a) Normalized magnitude of spatial gradient of the radial velocity vector at 350 km depth, along with plate reconstruction at 200 Ma. (b) Same as that in Figure 4a, but at 180 Ma. (c–g) (left) The evolution of the mantle temperature and flow field for the profile marked in red (top row) at labeled ages; (right) the same for the zoomed-in inset (within the radial arc segments on the left-hand side). The velocity vectors are normalized by the corresponding maximum velocity magnitude in each figure.

condition. We adopt case M5 ($\Delta\rho_{ch} = 3.5\%$, $\Delta d = 100$ km) as our reference model and describe it in more detail, since the buoyancy ratio, B, is comparable to that used in earlier studies [*Nakagawa and Tackley*, 2005; *Tan et al*., 2011; *Steinberger and Torsvik*, 2012]. Moreover, the thickness of the dense layer is volumetrically comparable to estimates of the volume of LLSVPs [*Hernlund and Houser*, 2008; *Burke et al*., 2008]. The flow regime in models with a chemically anomalous lower mantle is fundamentally different in the deep lower mantle, compared to that in cases with an isochemical lower mantle. For comparison with the purely

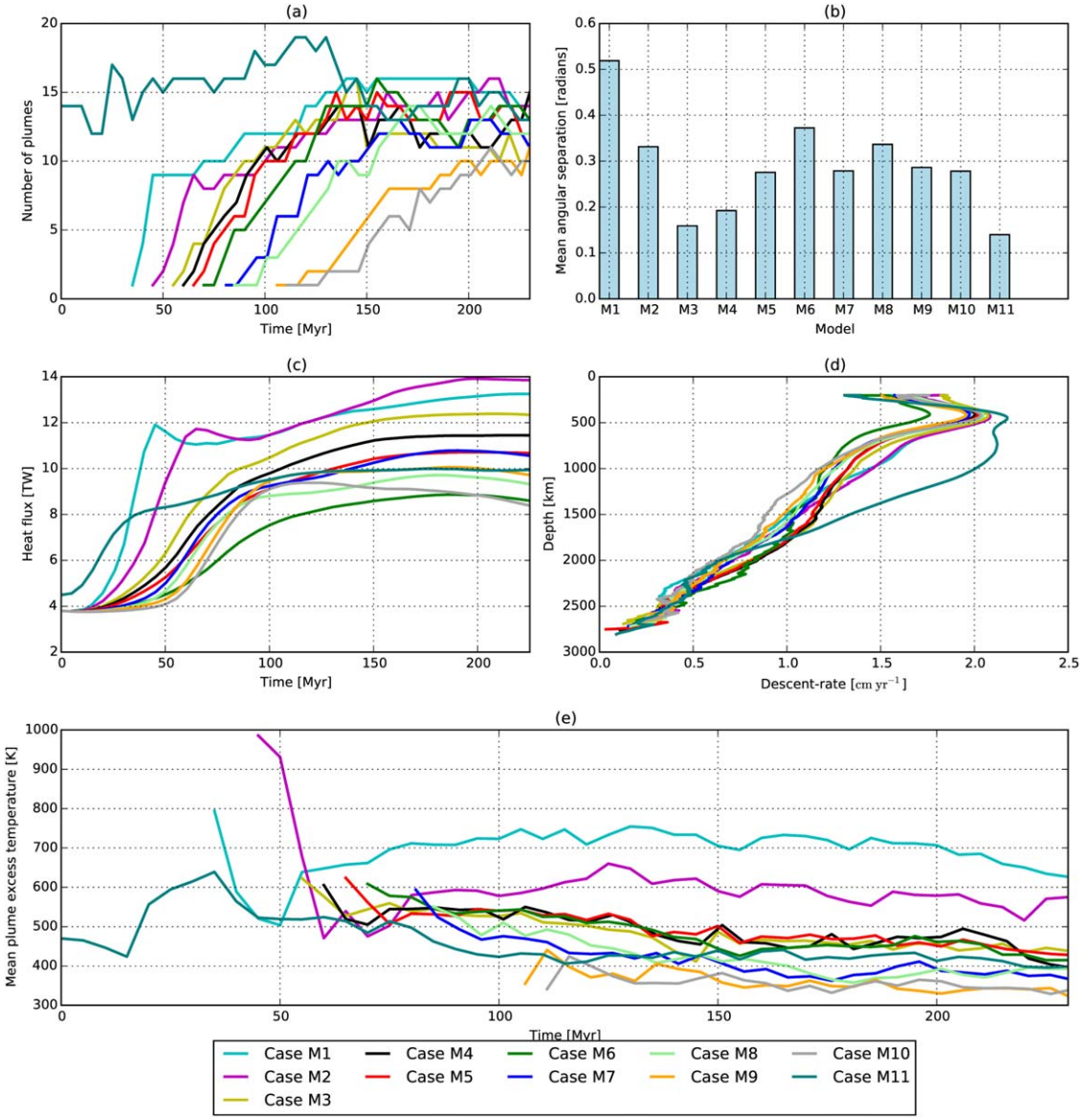

Figure 5. (a) Evolution of the number of plumes at 5 Myr time intervals for each model. (b) Mean angular separation of all plume eruption locations for each model. (c) Evolution of the CMB heat flux for each model. (d) Slab descent rates for each model. (e) Evolution of the mean plume excess temperature for each model.

thermal model (M1), we show the development and subsequent eruption of a plume beneath Greenland at 145 Ma (Figure 7). A total of 26 plume eruptions were detected in case M5, most of them appearing within the first 120 Myr of model time (Figure 5a) and with a total of 12 plumes surviving to the present-day (Table 2). The transit times of these plumes from the CMB to the surface range between 20 and 25 Myr. In contrast to plumes being rooted on the CMB as in case M1, plumes in models with a chemically anomalous lower mantle become anchored to topographic ridges of the dense layer, consistent with the laboratory results [*Jellinek and Manga*, 2002]. The dense layer gets swept into a network of circular embayments, separated by sharp ridges with plumes pinned to the peaks of these ridges. The dense chemical layer gradually thickens as shown with a black contour representing the 75% anomalous chemical concentration in Figure 7 and as a consequence its areal extent is reduced.

The partitioning of convection at the chemical interface through shear coupling is visualized in Figures 7c and 7f (see zoomed-in inset). Buoyant material rises along the sloping interfaces which feeds the conduit anchored to the peak of the chemical ridge. The reduced plume excess temperature at 350 km depth and

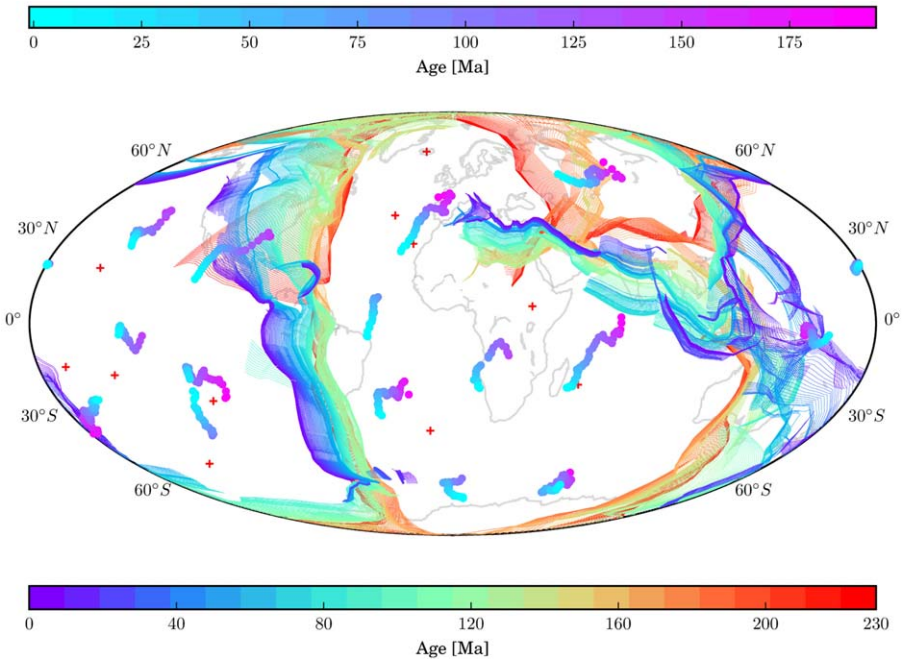

Figure 6. Location of subduction zones throughout the last 230 Myr, with age-coded paths that represent the lateral motion of plume conduits at a depth of 350 km since their eruption for case M1. Red "plus" symbols denote hotspots of deep origin.

that of CMB heat flux (Figures 5e and 5c) is a consequence of the dense chemical layer thermally shielding the mantle from the core [*Farnetani*, 1997].

The total number of plumes that survive to the present-day in these models ranges between 10 and 15. Increasing the initial thickness of the dense layer results in delayed plume eruptions, e.g., in case M10, with a 200 km thick dense layer, the first plume erupts after 110 Myr of model time (Figure 5a). Increasing the thickness and/or the buoyancy ratio, *B*, also results in a decrease in the CMB heat flux (Figure 5c) due to an increase in the internal temperature of the chemical structures and consequently in the reduction of the plume excess temperature at 350 km depth (Figure 5e).

With a small intrinsic density contrast of 1.25%, the dense layer in case M2 is easily entrained and almost completely eroded: the model essentially behaves similarly to case M1, with large plume excess temperatures at a depth of 350 km (Figure 5e). Cases M3 and M4, with intrinsic density contrasts of 2.5 and 3%, respectively, exhibit sheet-like upwellings and plume conduits reaching to a depth of 350 km are more tightly spaced (Figure 5b). Additionally, we find that increasing the thickness and/or the buoyancy ratio, *B*, results in lower slab sinking rates (Figure 5d) in the upper mantle, followed by a subsequent increase in the sinking rate in the deep lower mantle, relative to the sinking rates in case M1. In all our models, plume conduits migrate from their initial eruption locations in response to large-scale subduction-induced flow. The distances traversed by the plume conduits range between 1000 and 2000 km, similar to that observed in *Steinberger and Torsvik* [2012]. Since our model plumes remain active for periods longer than 100 Myr since their eruption, the speed of this motion is consistent with observations and earlier studies based on hotspot motion models for most hotspots [*Steinberger*, 2000].

The plume conduits in case M5 are long-lived and their roots, anchored to the peaks of chemical ridges, migrate laterally as the geometry of the network of ridges and embayments in the dense layer adjust to slab push forces. This is consistent with previous laboratory results [*Davaille et al*., 2002]. Plume conduits anchored to peaks of chemical ridges migrate laterally, as visualized in Figure 8, which shows the topography of the 75% chemical concentration isosurface at present-day along with the evolution of its edges since 180 Ma (Figure 8a). The plume buoyancy fluxes for numbered plumes that survive to the present-day are tabulated in Figure 8a. A 3-D perspective image (Figure 8b) shows well how plumes at present-day are pinned to the peaks of chemical ridges.

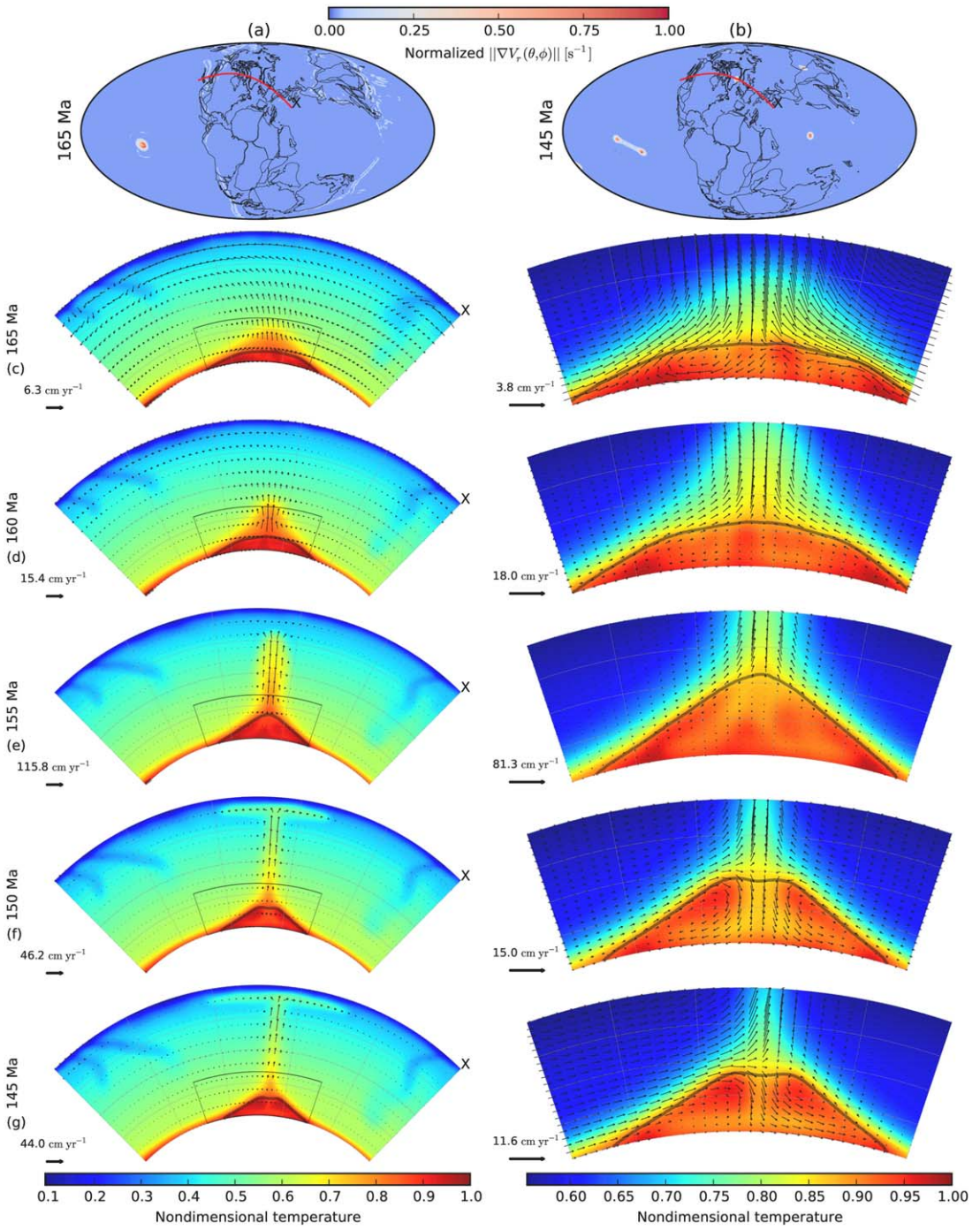

Figure 7. (a) Normalized magnitude of spatial gradient of the radial velocity vector at 350 km depth, along with plate reconstruction at 165 Ma. (b) Same as that in Figure 7a, but at 145 Ma. (c–g) (left) The evolution of the mantle temperature and flow fields for the profile marked in red (top row) at labeled ages; (right) the same for the zoomed-in inset (within the radial arc segments on the left-hand side). The thick black contours represent the 75% anomalous chemical concentration. The velocity vectors are normalized by the corresponding maximum velocity magnitude in each figure.

The initial distribution (at 230 Ma) of chemical heterogeneity in cases M2–M10 is "least-biased" because the dense layer has uniform thickness. However, prior to the Mesozoic, the dense layer may have already been displaced and deformed by slabs, and plumes erupted from the CMB. Therefore, we initiate a case (M11) at 230 Ma that contains preexisting plumes and a deformed chemical layer to investigate the influence of the initial condition on the spatiotemporal distribution of plume eruptions from 230 Ma to present-day. The

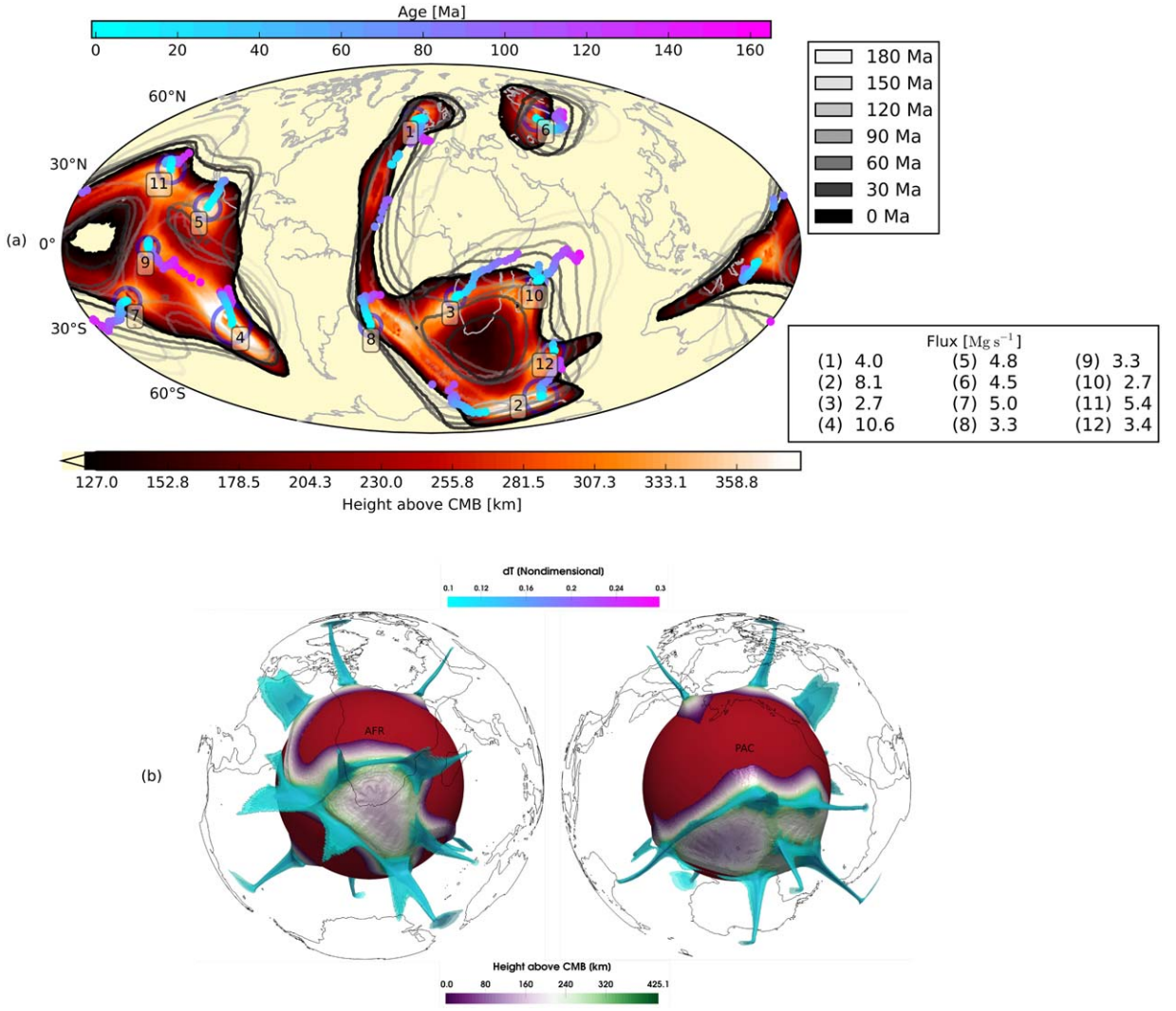

Figure 8. (a) Topography of the 75% chemical concentration isosurface, above the CMB at present-day for case M5. Contour lines show the evolution of the areal extent of the 75% chemical concentration isosurface since 180 Ma to present-day. Age-coded plume paths at a depth of 350 km are shown in the foreground and plumes at present-day are numbered. Radii of blue circles encircling present-day plumes are representative of their respective buoyancy fluxes, which are listed in the frame to the right. (b) The temperature field above layer averages, δT, is plotted as isosurfaces in the range 0.1–0.3, delineating plume conduits at present-day for case M5. Topography of the 75% chemical concentration isosurface, above the CMB, is also shown for the same model at present-day. Coastlines are shown for geographical reference.

initial condition in case M11 uses the thermochemical heterogeneity from case M5 at 75 Ma (Figure 8a). Figure 12a shows the locations of 14 plumes in the initial condition for case M11, marked by black hexagons.

A total of 49 plume eruptions were detected in this model and a total of 13 plumes survive to the present-day (Table 2). The longevity of plume conduits is similar to that observed in cases M2–M10. A notable feature of case M11 is the considerably higher slab descent rate in the shallow lower mantle (Figure 5d), which is most likely due to the preexisting flow structure within the mantle in the initial condition.

A more rigorous assessment of the sensitivity to initial conditions is carried out using model M5L, described in more detail in the following section.

3.3. Influence of Initial Conditions

In order to carry out a more robust assessment of the influence of initial conditions on model plume eruption locations, we initiate two models—one with an isochemical lower mantle (M1L) and the other with a chemically anomalous lower mantle (M5L)—that each span a total of 730 Myr of integrated model time. The initial conditions for models M1L and M5L are derived from convection calculations that are

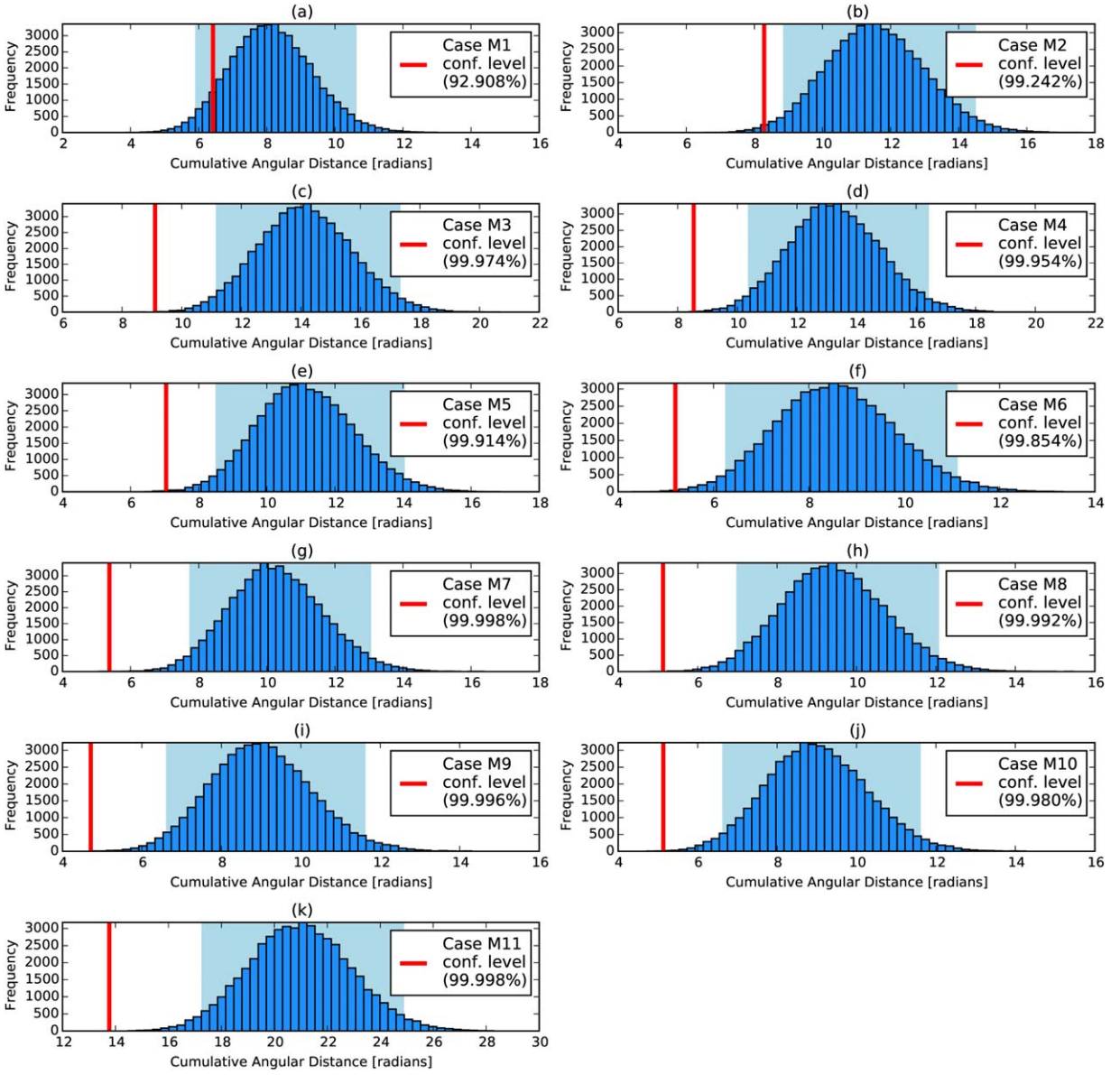

Figure 9. (a–k) Cumulative distances obtained from 50,000 Monte Carlo realizations (described in section 2.6)—split into 50 bins—for each model (M1–M11). In each figure, the 95% confidence interval is shaded in light blue and the red line shows the cumulative angular distance obtained for the corresponding model.

parameterized the same way as models M1 and M5, respectively, but with free-slip boundary conditions. We run the free-slip convection models for 500 Myr, which is about twice the typical timescale for slabs to descend from the surface to the CMB and about 20–30 whole mantle transit times for the plumes. The free-slip convection models reach a statistically steady state well within 500 Myr of model time, featuring an unbiased distribution of plumes. At 230 Ma, slabs are imposed on the temperature fields obtained from these free-slip convection models to produce the initial conditions for M1L and M5L. For M5L, the initial thermochemical heterogeneity above the CMB is obtained from the corresponding free-slip convection model, where the initially uniform thermochemical layer has deformed significantly after 500 Myr.

We allow $\approx$1 plume transit time of 15 and 25 Myr for the plumes in models M1L and M5L, respectively, to adjust to subduction-induced large-scale flow since 230 Ma and only record plume eruptions after this adjustment period. This is a reasonable approach since some plumes in the initial condition of these models are adjacent to subduction zones at 230 Ma, which is physically improbable. Plumes in the initial condition

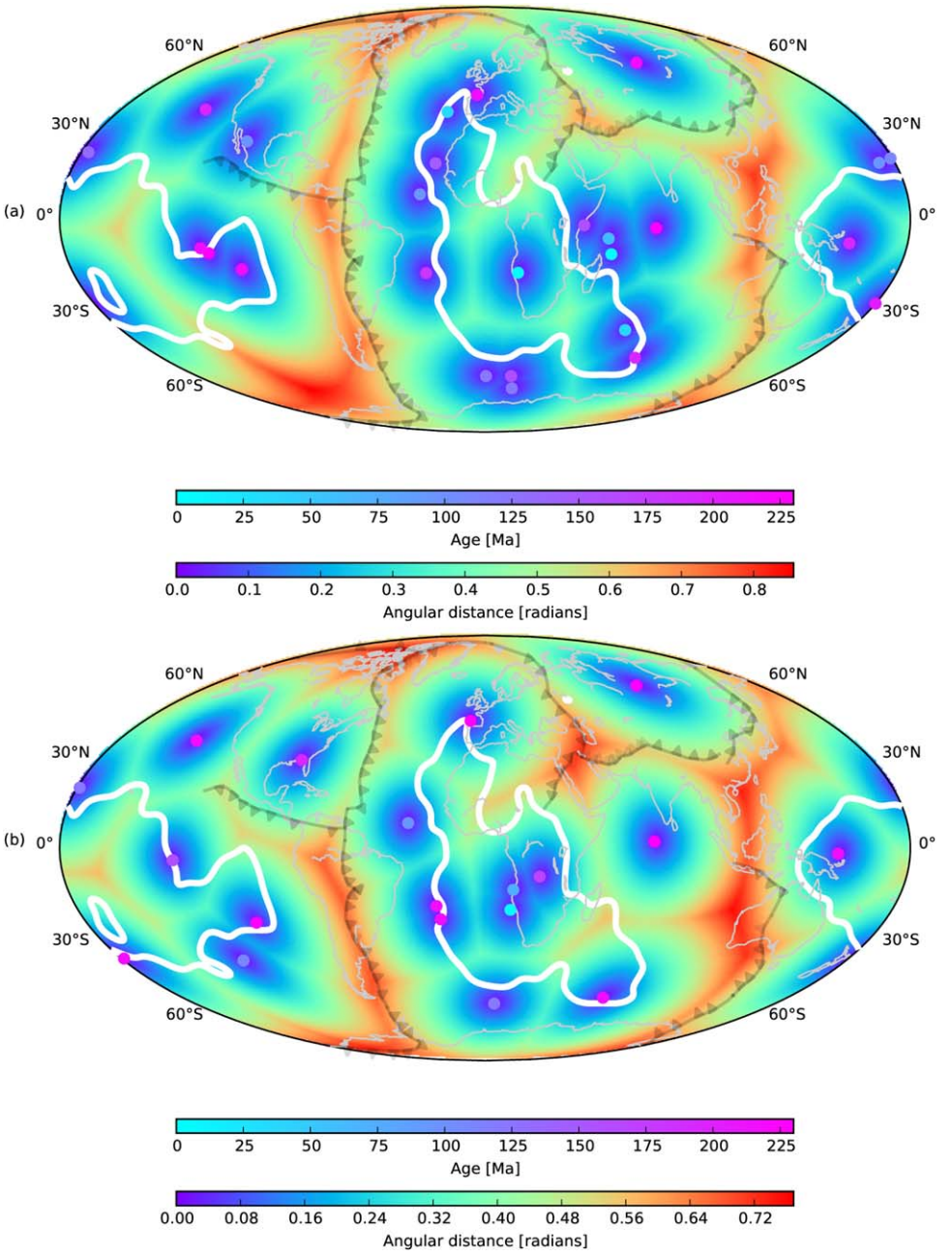

Figure 10. (a) Age-coded model plume eruption locations for case M5, with angular distance to the closest model plume eruption location shown in the background. The 1% slow shear wave velocity contour in the SMEAN tomographic model is shown in white. The location of subduction zones at 230 Ma is shown in black to illustrate the influence of subduction history on the preferential origin of plumes. (b) Same as in Figure 10a but for case M1.

of models M1L and M5L are marked by black hexagons and subsequent eruptions are shown in Figures 13b and 13a, respectively. A total of 85 and 69 plume eruptions were detected in models M1L and M5L, respectively, where 21 and 16 plumes survive to the present-day, respectively.

3.4. Statistical Analyses

For models M1–M11, results from the Monte Carlo statistical analysis of model plume eruptions, based on the method described in section 2.6, are shown in Figure 9. We find that the model plume eruption locations for models with a chemically anomalous lower mantle (M2–M11) are highly correlated with reconstructed LIP eruptions sites. Moreover, plume eruption locations in model M5L, initiated with an unbiased

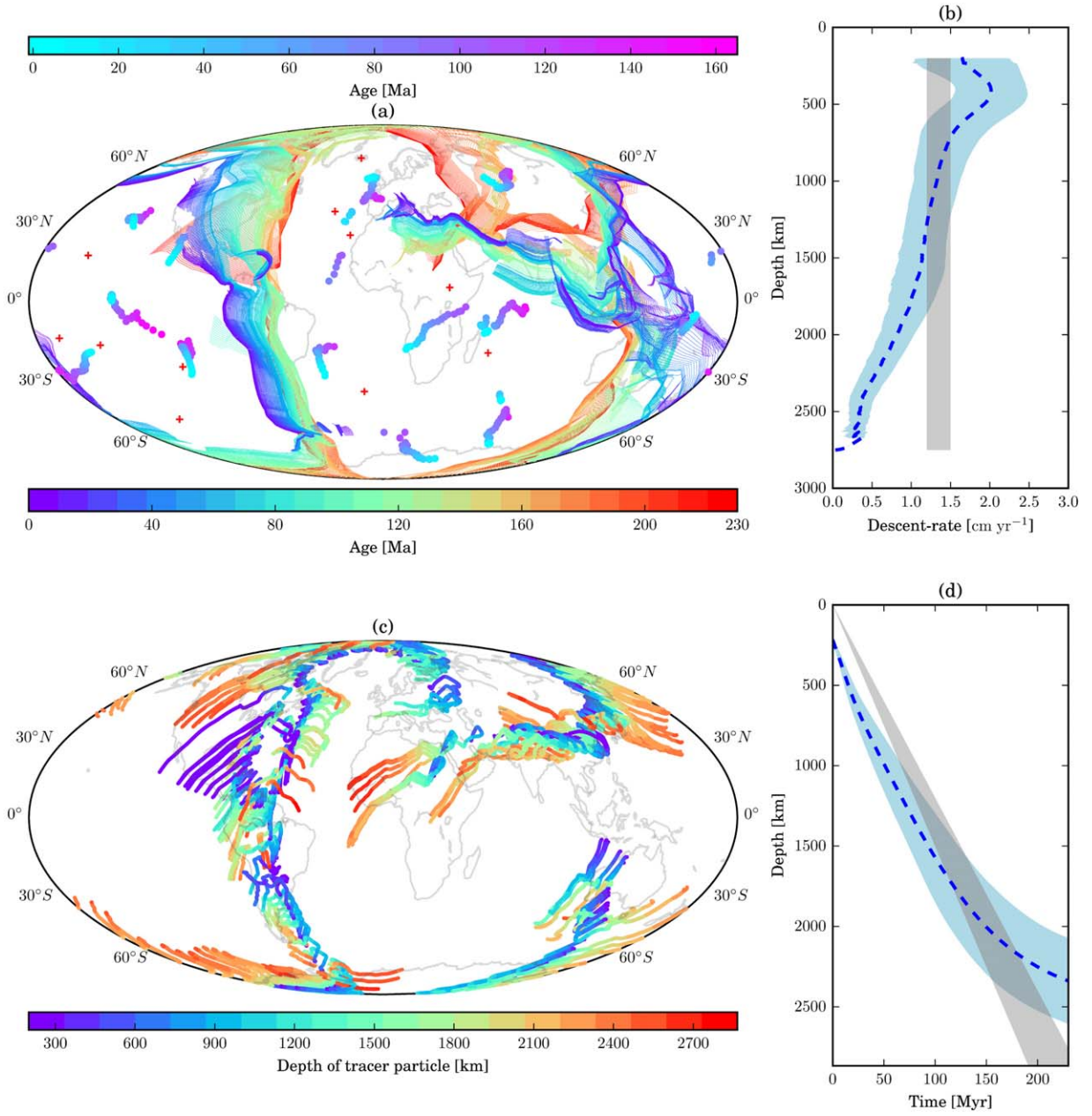

Figure 11. Model results for case M5. (a) Location of subduction zones throughout the last 230 Myr, with age-coded paths that represent the lateral motion of plume conduits at a depth of 350 km since their eruption. Red "plus" symbols denote hotspots of deep origin. (b) Mean slab descent rate for all tracer particles, with $\pm 1\sigma$ shaded in blue and estimates from *Van der Meer et al.* [2009] shaded in grey. (c) Depth-coded trajectories of descending slab material, starting at 200 km depth (see Figure 2a). (d) Mean age-depth relationship for all tracer particles, with $\pm 1\sigma$ shaded in blue and estimates from *Van der Meer et al.* [2009] shaded in grey.

distribution of plumes and a deformed thermochemical layer, is also highly correlated with LIP eruption sites (Figure 13c). The correlation coefficient obtained for model M1, however, has a confidence level of 92.9%, falling just short of the 95% confidence level (Figure 9a). The lower confidence level obtained for case M1 is a consequence of its large mean angular separation of plume eruption locations (Figure 5b), compared to models with a chemically anomalous lower mantle (M2–M11). We also find that the correlation coefficient obtained for model M1L, initiated with an unbiased distribution of plumes, falls well short of the 95% confidence level (Figure 13d).

To better appreciate the correlation, we show the plume eruption locations for cases M5 and M11, plotted as individual points around the 1% slow shear wave velocity contour in the SMEAN tomographic model in

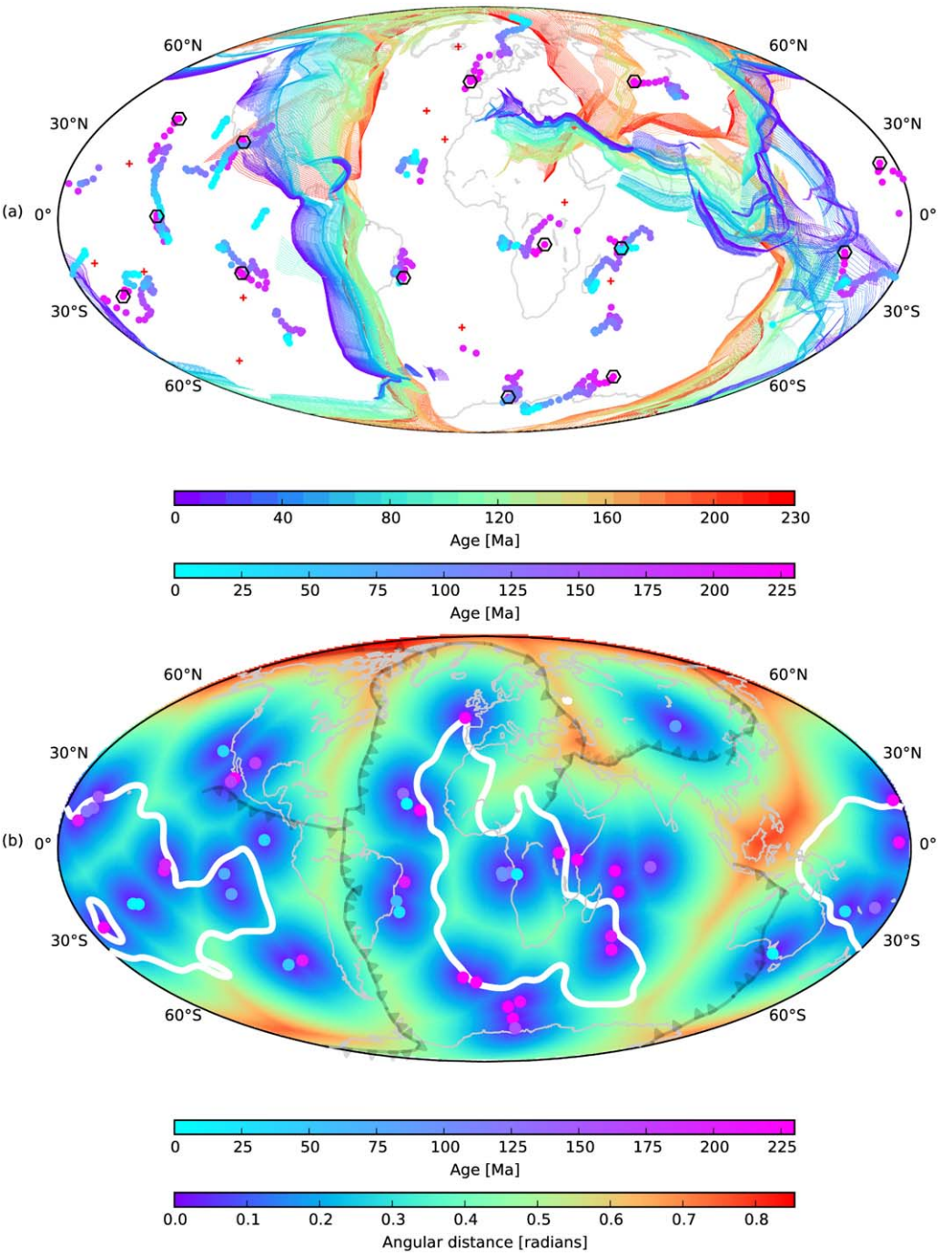

Figure 12. (a) Location of subduction zones through the last 230 Myr, with age-coded paths that represent the lateral motion of plume conduits at a depth of 350 km since their eruption for case M11. Red "plus" symbols denote hotspots of deep origin. Black hexagons represent the location of plume conduits at a depth of 350 km in the initial condition—see in text for more details. (b) Age-coded model plume eruption locations for case M11, with angular distance to the closest model plume eruption location shown in the background. The 1% slow shear wave velocity contour in the SMEAN tomographic model is shown in white. The location of subduction zones at 230 Ma is shown in black to illustrate the influence of subduction history on the preferential origin of plumes.

Figures 10a and 12b, respectively. The distance to the nearest plume eruption location (background shading of Figures 10a and 12b), when compared to Figures 11 and 8a, demonstrates the first-order role that subduction history plays in shaping the geometry and dictating the location of the LLSVPs [*McNamara and Zhong*, 2005] and consequently in triggering the preferential origin of plumes from the edges of the LLSVPs. Figure 10b shows the plume eruption locations for case M1, with distance to the nearest plume eruption

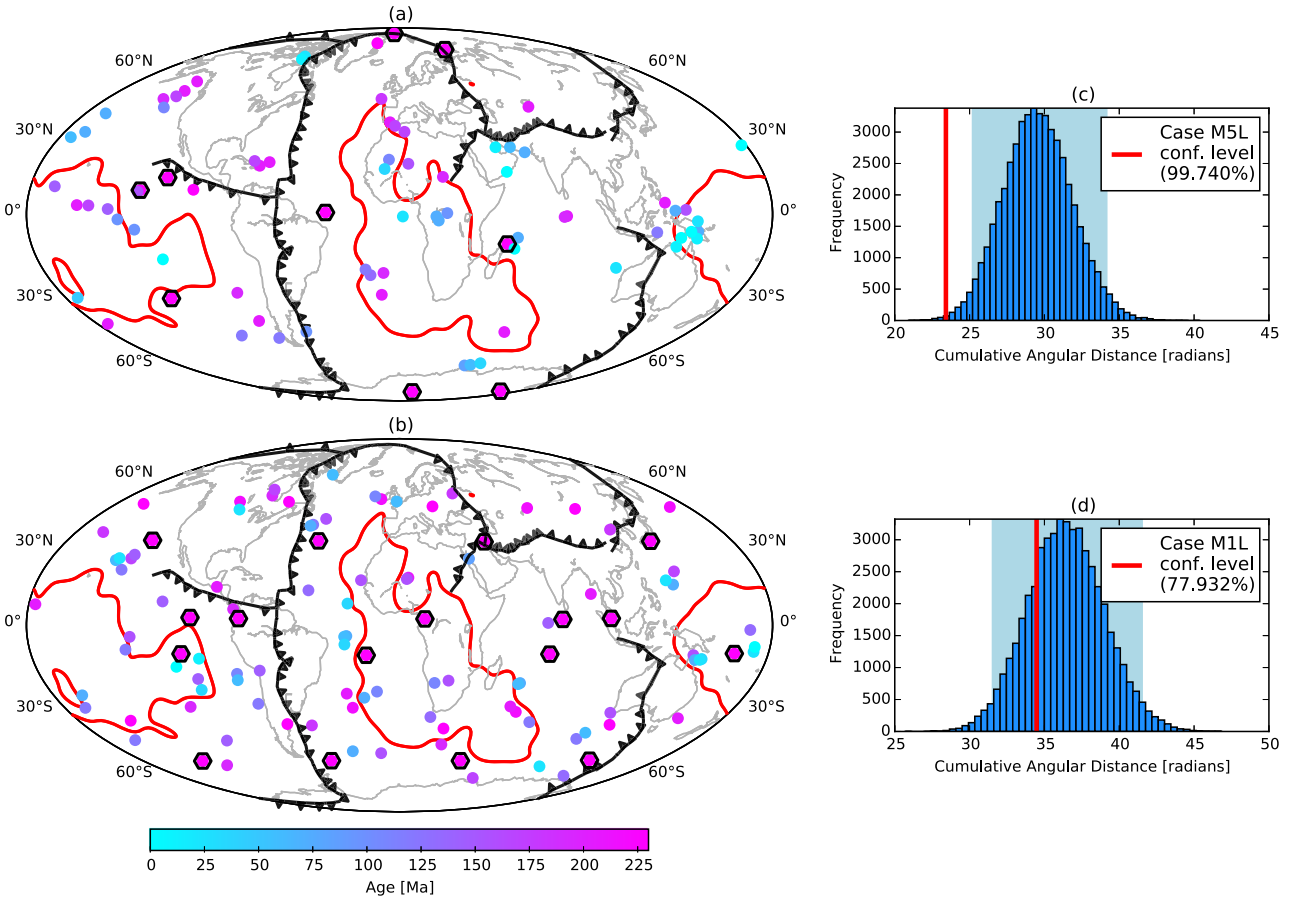

Figure 13. (a) Age-coded model plume eruption locations for case M5L, with plumes in the initial condition marked by black hexagons. The 1% slow shear wave velocity contour in the SMEAN tomographic model is shown in red. The location of subduction zones at 230 Ma is shown in black and present-day coastlines are shown for reference. (b) Same as that in Figure 13a, but for model M1L. (c) Same as those in Figure 9, but for model M5L. (d) Same as that in Figure 13c, but for model M1L.

location in the background. Plume eruption locations in this model are not as tightly laid out around the 1% slow shear wave velocity contour as that in models with a chemically anomalous lower mantle and as a consequence the correlation coefficient obtained from the Monte Carlo statistical test for this case fails to exceed the 95% confidence level.

4. Discussion

4.1. Morphology of Thermochemical Structures

In models with a chemically anomalous lower mantle, the dense layer thickens in response to large-scale subduction-induced flow and gets swept into a network of circular embayments, separated by sharp ridges. In this network of embayments and ridges, plumes get anchored to the peaks of the ridges [*Davaille et al.*, 2005]. The temporal evolution of the chemical structures is guided by slab push forces on the one hand and the gradual erosion resulting from entrainment on the other hand.

Figure 11a shows trails of plume conduits in case M5 at a depth of 350 km in relation to the location of subduction zones over the last 230 Myr and the present-day hotspots of deep origin [*Steinberger*, 2000] are shown in red "plus" symbols. The general pattern of the trails of plume conduits in the corresponding figure for case M11 (Figure 12a) is similar to that in case M5, although the trails in the former are longer due to the presence of plumes throughout the entire model time, spanning the last 230 Myr.

Slab sinking rates (Figure 11b) and slab age-depth relationship in case M5 (Figure 11d) are comparable to the published estimates [*Van der Meer et al.*, 2009]. However, our models show a gradual decline of slab

sinking rates as slabs approach the CMB. The depth-coded trajectories of sinking slabs, based on the method described in section 2.4, are shown in Figure 11c.

Although given the length scales associated with the entrainment process are much smaller than we can resolve in our numerical models to provide a quantitatively accurate description of entrainment [*McNamara and Zhong*, 2004], our general qualitative description of the shape of the LLSVPs through time should still hold. The gradual shrinkage of the Pacific LLSVP in case M5 (Figure 8a) since 180 Ma is partly through the effects of entrainment, however, its northernmost edge near present-day southwestern Canada recedes rapidly southward in response to strong slab push forces (Figure 11c). To a larger extent, the morphology of the African LLSVP is guided by slab push forces, causing its easternmost edge to recede rapidly from 180 Ma to the tip of present-day Madagascar and its ridge-like shape in the north-south direction is a consequence of slab material from the Africa-Eurasian collision pushing the chemical layer southward. An overall shrinkage of the African LLSVP through time is also observed due to entrainment.

The mean angular distance between LIPs and hotspots used in this study is ≈1000 km. The mean angular distance between model plume eruptions for cases with a chemically anomalous lower mantle (M2–M11) range between 1000 and 2400 km. *Jellinek and Manga* [2002] showed, based on linear stability theory, that the horizontal spacing between conduits can be obtained by

$$L \approx \frac{20\pi D_m}{C}\left(\frac{\lambda_h}{Ra}\right)^{1/3}, \tag{14}$$

where L, D_m, and λ_h are the conduit separation, thickness of the mantle, and the ratio of ambient viscosity to that of the bottom TBL, respectively. C is a constant (≈0.6), which depends on λ_h and buoyancy ratio, B. Conduit separation according to linear stability theory is ≈1800 km. We therefore speculate that the observed clustering of LIP eruption sites around the present-day LLSVPs is a dynamic consequence of the network of ridges and embayments extant within them. Even though equation (14) is not strictly applicable, since C is not well constrained and the model geometries are different, we contend that it should still provide a rough estimate, given that Ra and λ_h in this study are comparable to that in *Jellinek and Manga* [2002]. Our analysis is in agreement with *Burke et al*. [2008] who suggested that temperature gradients across steep margins of the LLSVPs are a key control for the generation of plumes. However, our models suggest that the temperature gradients are not limited to the edges of the LLSVPs, particularly in the case of the Pacific LLSVP, where the network of ridges extends into its interior.

Davies et al. [2015] suggested that the spatial correlation of hotspots and reconstructed LIPs with the edges of the African LLSVP is a consequence of its elongated shape. Our models suggest that this spatial correlation is likely a consequence of the characteristic separation between conduits, imposed by the network of ridges in the deep lower mantle. Consequently, the morphological differences between the network of ridges extant in the African and the Pacific LLSVPs are likely to be related to their respective geometries.

We also find that a plume emerging from the edge of the Pacific LLSVP can migrate toward its interior, whilst being anchored to a topographic ridge on the LLSVP, e.g., the plume labeled 9, in Figure 8a. This is consistent with the results from earlier models, e.g., *Steinberger and Torsvik* [2012].

4.2. Plume Buoyancy Flux

Temperature dependence of viscosity causes large decreases in viscosity within plume conduits, resulting in large velocities of plume material within the conduits. Since we explicitly limit viscosity variation to ≈1400X, in order to avoid numerical difficulties in the solvers, we cannot fully capture the large viscosity reductions within plume conduits such as in case M1, due to the large temperature differential between plume material and the ambient mantle, exceeding 600 K at a depth of 350 km (Figure 5e). Hence, conduit velocities for case M1 and case M5 (Figures 7 and 4) appear similar, even though conduit temperatures in case M1 are much higher compared to that in case M5. However, previous studies have shown that plume excess temperatures in purely thermal models are consistent with observations [*Bunge*, 2005; *Leng and Zhong*, 2008]. It is likely that plume excess temperatures in case M1 are large partly because of a weaker depth-dependence of thermal expansivity, compared to these earlier studies, and the rapid ascent of plumes due to strong depth and temperature dependence of viscosity.

The plume buoyancy fluxes—computed as described in Appendix A—for case M5 (Figure 8a) are comparable to that of present-day estimates for strong plumes, e.g., the Hawaiian plume. The total plume heat flux and buoyancy flux at present-day, at a depth of 350 km, for case M5 is ≈2.3 TW and ∼57.8 Mg s^{-1}, respectively, and are comparable to estimates from *Sleep* [1990], although his estimates include more plumes. The total plume heat flux for case M5 is about 22% of the CMB heat flux. To what extent plume heat flux is representative of core heat flux is uncertain [*Zhong*, 2005], although estimates from earlier studies [*Zhong*, 2006] suggest that plume heat flux account for ≈80% of the CMB heat flux. However, a small ratio of plume heat flux to core heat flux is not unexpected, since the dense layer above the CMB essentially prevents the lower part of the bottom TBL from becoming entrained by the plume [*Farnetani*, 1997] (Figures 7 and 4). Thermochemical plumes are preferred over purely thermal plumes as their strengths and excess temperatures are more consistent with observations [*Davaille et al*., 2003, 2002].

4.3. Statistical Analysis of Model Plume Eruptions

Subduction history plays a key role in shaping the geometry and dictating the location of the LLSVPs [*McNamara and Zhong*, 2005], consequently causing plumes to emerge preferentially from their margins (Figure 10a). We start all our models with slabs initially inserted from the surface to a depth of 1200 km. The initial depth of slabs influences the timing of the emergence of plumes; however, we do not expect the pattern of plumes emerging from the edges of the LLVSPs to change for different initial slab depths. Initiating models with slabs inserted to a shallower depth is most likely to result in a delayed thickening of the dense layer for cases (M2–M10)—where the chemically anomalous layer above the CMB is of uniform thickness in the initial condition—and thus lead to a longer incubation period for incipient plumes. We also expect a similar behavior for case M1.

Plume eruptions in models with a chemically anomalous lower mantle (M2–M11 and M5L) are highly correlated with LIP eruption sites. Moreover, in contrast to *Steinberger and Torsvik* [2012], where a model case with preexisting plumes was not as successful in reproducing the pattern of plumes emerging from the edge of the LLSVPs, we find that in analogous model cases, M11 and M5L, plumes emerge preferentially from the edges of the LLSVPs, with only a small percentage emerging from their interiors. The Pacific LLSVP in Figure 12b features a number of eruptions within its interior, which originate from the network of ridges that runs deep into its interior. It is likely that our conclusions from case M11 and M5L differ from that in *Steinberger and Torsvik* [2012], partly because our models include lateral viscosity variations.

However, the confidence level for case M1 fails to exceed the 95% level due to the larger mean angular separation of plume eruption sites in the model. Plume spacing and number is shown to be controlled by the Rayleigh number, *Ra*, and the thickness of the lower TBL, δ. *Zhong* [2005] showed thermal plumes in isoviscous models with $3\times10^6 \leq Ra \leq 3\times10^7$, where plume number scales as $Ra^{0.31}$ and plume spacing as $\approx \delta^{1/2}$. Since *Ra*, based on the thickness of the mantle, is of the same order in our models ($\approx 4.5\times10^7$), it is possible that a larger confidence level can be obtained for models with purely thermal plumes by varying *Ra* and/or the thickness of the bottom TBL. Future studies should further explore the parameter space of models with purely thermal plumes in this regard.

Moreover, the confidence level for model M1L, initiated with an unbiased distribution of plumes, falls well short of 95%. This does not necessarily preclude the possibility of purely thermal plumes, since the unbiased distribution of plumes in the initial condition of this model is unlike a distribution of plumes that would result from subduction history prior to the Mesozoic. Future studies should aim to systematically study lower mantle reorganization timescales in the absence of a dense thermochemical layer above the CMB.

Model M5L further reinforces our inferences by demonstrating that in the presence of a dense thermochemical layer above the CMB, preexisting plumes drawn from an unbiased distribution swiftly adjust their locations as the thermochemical layer morphs—likely guided by the dynamical constraints we outlined in section 4.1—in response to subduction-induced large-scale flow and subsequent plumes emerge preferentially from the edges of thermochemical structures. Model M5L also demonstrates that our results for models with a chemically anomalous lower mantle are robust—at least within the parameter space studied here—and that such models are not particularly sensitive to initial conditions.

The viscosity of the deep mantle is not well constrained and is likely to vary substantially due to variations in temperature, pressure, phase, chemistry, and grain size—see *Tackley* [2012] for a detailed discussion. *McNamara and Zhong* [2004] showed that isolated, rounded plume structures can form if the dense material above the CMB is more viscous—although their study did not include the effect of subduction. The influence of an intrinsic viscosity contrast of the dense material, not considered in this study, therefore needs to be investigated further. However, we do not expect the statistical analysis presented here to be strongly affected, since subduction history plays a first-order role in shaping the geometry of the dense layer [*McNamara and Zhong*, 2005] and consequently in causing plumes to emerge preferentially from the edges of thermochemical structures.

5. Conclusion

We have presented global convection models that span the last 230 Myr, with paleogeographically constrained slab subduction, in which plumes emerge preferentially near the edges of thermochemical structures that resemble present-day LLSVPs. The total number of plumes that survive to the present-day ranges between 10 and 15, consistent with the findings from earlier studies, e.g., *Zhong* [2005] and *Steinberger and Antretter* [2006]. Furthermore, *Davaille et al*. [2005] suggested that at any time the Indo-Atlantic domain should contain about 3–9 instabilities at different stages of their development, which is consistent with the models presented in this study.

We also present a novel plume detection scheme based on *k*–means clustering, which is robust in its ability to discriminate between shallow temperature anomalies and that of legitimate plume conduits. The new plume detection scheme is robust in its ability to cope with variations in plume excess temperatures and radial velocities within conduits for model plumes at different stages of their development. Based on this plume detection scheme, we present Monte Carlo-based statistical analyses that suggest that plume eruptions in models with a chemically anomalous lower mantle are highly correlated to LIP eruption sites, whereas the confidence level obtained for a model with purely thermal plumes falls short of the 95% confidence level. We also demonstrate that model plumes become anchored to topographic highs on thermochemical structures that resemble the shape of present-day LLSVPs. Based on these results we suggest that the observed clustering of LIP eruption sites around the present-day LLSVPs is a dynamic consequence of the network of ridges and embayments extant within them, which control the location of plumes.

Appendix A: Plume Buoyancy Flux

At a given time, we compute the horizontally averaged temperature at each radial shell, $T_{ave}(r)$. We then compute a similar quantity, $T_{bg}(r)$, which is the horizontally averaged temperature at each radial shell excluding cold material, i.e., the horizontal average of temperature such that $T(r) > T_{ave}(r)$. Since plume excess temperatures are measured relative to upper mantle temperature away from subduction zones, we adopt the approach taken in *Zhong* [2006] and compute plume buoyancy fluxes relative to $T_{bg}(r)$.

For each plume, identified by the plume detection scheme (section 2.5) at a given time, we compute the standard deviation, σ, of the radial velocity, $V_r(\theta, \phi)$, at a depth of 350 km, within a 400 km radius of the conduit center. We then use an isocontour $(max(V_r(\theta, \phi)) - 2\sigma)$ to mark the edge of a conduit, Γ. This approach constrains conduit radii to ≈100–150 km and effectively excludes the thermal halo around plume conduits, making them consistent with estimates of plume radii in the upper mantle [*Sleep*, 2006]. *Sleep* [2006] also suggests that the distance from the plume radius to the edge of the thermal halo is around 100 km in the upper mantle, which is roughly the amount of "trimming" achieved by the above procedure. We then numerically integrate the following equation to compute the buoyancy flux associated with a plume at a depth of 350 km:

$$\int_{\Gamma} \rho\alpha(T - T_{bg})V_r. \tag{A1}$$

Acknowledgments
We obtained CitcomS (version 3.2) from the Computational Infrastructure for Geodynamics (http://geodynamics.org/). GPlates (http://www.gplates.org/) is developed at the University of Sydney, the California Institute of Technology, and the Geological Survey of Norway. All figures in this paper have been made with Matplotlib [*Hunter*, 2007], except Figure 8b, made using ParaView [*Squillacote and Ahrens*, 2007]. We thank Rhodri Davies and Allen McNamara for comprehensive and insightful reviews. R.H. and N.F. were supported by Statoil ASA. D.M., N.F., and R.H. were also supported by ARC grant IH130200012. M.G. and D.J.B. were partially supported by Statoil ASA and the NSF (through EAR-1161046 and EAR-1247022). This research was undertaken with the assistance of resources from the National Computational Infrastructure (NCI), which is supported by the Australian Government.

References

Artemieva, I. M. (2006), Global 1× 1 thermal model tc1 for the continental lithosphere: Implications for lithosphere secular evolution, *Tectonophysics*, *416*(1), 245–277.
Austermann, J., B. T. Kaye, J. X. Mitrovica, and P. Huybers (2014), A statistical analysis of the correlation between large igneous provinces and lower mantle seismic structure, *Geophys. J. Int.*, *197*(1), 1–9.
Besag, J., and P. J. Diggle (1977), Simple Monte Carlo tests for spatial pattern, *Appl. Stat.*, *26*(3), 327–333.
Boschi, L., T. Becker, and B. Steinberger (2007), Mantle plumes: Dynamic models and seismic images, *Geochem. Geophys. Geosyst.*, *8*, Q10006, doi:10.1029/2007GC001733.
Bower, D. J., M. Gurnis, and M. Seton (2013), Lower mantle structure from paleogeographically constrained dynamic Earth models, *Geochem. Geophys. Geosyst.*, *14*, 44–63, doi:10.1029/2012GC004267.
Bower, D. J., M. Gurnis, and N. Flament (2015), Assimilating lithosphere and slab history in 4-D Earth models, *Phys. Earth Planet. Inter.*, *238*, 8–22, doi:10.1016/j.pepi.2014.10.013.
Boyden, J. A., R. D. Müller, M. Gurnis, T. H. Torsvik, J. A. Clark, M. Turner, H. Ivey-Law, R. J. Watson, and J. S. Cannon (2011), Next-generation plate-tectonic reconstructions using gplates, *Geoinformatics: Cyberinfrastructure for the Solid Earth Sciences*, pp. 95–114, Cambridge University Press, Cambridge, U. K.
Bunge, H.-P. (2005), Low plume excess temperature and high core heat flux inferred from non-adiabatic geotherms in internally heated mantle circulation models, *Phys. Earth Planet. Inter.*, *153*(1), 3–10.
Burke, K., and T. H. Torsvik (2004), Derivation of large igneous provinces of the past 200 million years from long-term heterogeneities in the deep mantle, *Earth Planet. Sci. Lett.*, *227*(3), 531–538.
Burke, K., B. Steinberger, T. H. Torsvik, and M. A. Smethurst (2008), Plume generation zones at the margins of large low shear velocity provinces on the core–mantle boundary, *Earth Planet. Sci. Lett.*, *265*(1), 49–60.
Campbell, I. H. (2007), Testing the plume theory, *Chem. Geol.*, *241*(3), 153–176.
Campbell, I. H., and R. W. Griffiths (1990), Implications of mantle plume structure for the evolution of flood basalts, *Earth Planet. Sci. Lett.*, *99*(1), 79–93.
Christensen, U. R., and A. W. Hofmann (1994), Segregation of subducted oceanic crust in the convecting mantle, *J. Geophys. Res.*, *99*(B10), 19,867–19,884.
Christensen, U. R., and D. A. Yuen (1985), Layered convection induced by phase transitions, *J. Geophys. Res.*, *90*(B12), 10,291–10,300.
Čížková, H., A. P. van den Berg, W. Spakman, and C. Matyska (2012), The viscosity of earths lower mantle inferred from sinking speed of subducted lithosphere, *Phys. Earth Planet. Inter.*, *200*, 56–62.
Coffin, M. F., and O. Eldholm (1994), Large igneous provinces: crustal structure, dimensions, and external consequences, *Rev. Geophys.*, *32*(1), 1–36.
Davaille, A., F. Girard, and M. Le Bars (2002), How to anchor hotspots in a convecting mantle?, *Earth Planet. Sci. Lett.*, *203*(2), 621–634.
Davaille, A., M. Le Bars, and C. Carbonne (2003), Thermal convection in a heterogeneous mantle, *C. R. Geosci.*, *335*(1), 141–156.
Davaille, A., E. Stutzmann, G. Silveira, J. Besse, and V. Courtillot (2005), Convective patterns under the Indo-Atlantic <<box>>, *Earth Planet. Sci. Lett.*, *239*(3), 233–252.
Davies, D., S. Goes, and M. Sambridge (2015), On the relationship between volcanic hotspot locations, the reconstructed eruption sites of large igneous provinces and deep mantle seismic structure, *Earth Planet. Sci. Lett.*, *411*, 121–130.
Deschamps, F., and P. J. Tackley (2008), Searching for models of thermo-chemical convection that explain probabilistic tomography: I. Principles and influence of rheological parameters, *Phys. Earth Planet. Inter.*, *171*(1), 357–373.
Ernst, R. E., and K. L. Buchan (2002), Maximum size and distribution in time and space of mantle plumes: Evidence from large igneous provinces, *J. Geodyn.*, *34*(2), 309–342.
Farnetani, C. (1997), Excess temperature of mantle plumes: The role of chemical stratification across D, *Geophys. Res. Lett.*, *24*(13), 1583–1586.
Flament, N., M. Gurnis, S. Williams, M. Seton, J. Skogseid, C. Heine, and R. Dietmar Müller (2014), Topographic asymmetry of the South Atlantic from global models of mantle flow and lithospheric stretching, *Earth Planet. Sci. Lett.*, *387*, 107–119.
Gonnermann, H. M., M. Manga, and A. Mark Jellinek (2002), Dynamics and longevity of an initially stratified mantle, *Geophys. Res. Lett.*, *29*(10), doi:10.1029/2002GL014851.
Gurnis, M. (1986), The effects of chemical density differences on convective mixing in the Earth's mantle, *J. Geophys. Res.*, *91*, 11,407–11,419, doi:10.1029/JB091iB11p11407.
Gurnis, M., M. Turner, S. Zahirovic, L. DiCaprio, S. Spasojevic, R. D. Müller, J. Boyden, M. Seton, V. C. Manea, and D. J. Bower (2012), Plate tectonic reconstructions with continuously closing plates, *Comput. Geosci.*, *38*(1), 35–42.
Hager, B. H., R. W. Clayton, M. A. Richards, R. P. Comer, and A. M. Dziewonski (1985), Lower mantle heterogeneity, dynamic topography and the geoid, *Nature*, *313*(6003), 541–545.
Hernlund, J. W., and C. Houser (2008), On the statistical distribution of seismic velocities in earth's deep mantle, *Earth Planet. Sci. Lett.*, *265*(3), 423–437.
Hunter, J. D. (2007), Matplotlib: A 2D graphics environment, *Comput. Sci. Eng.*, *9*(3), 90–95.
Ishii, M., and J. Tromp (1999), Normal-mode and free-air gravity constraints on lateral variations in velocity and density of earth's mantle, *Science*, *285*(5431), 1231–1236.
Ita, J., and S. D. King (1994), Sensitivity of convection with an endothermic phase change to the form of governing equations, initial conditions, boundary conditions, and equation of state, *J. Geophys. Res.*, *99*(B8), 15,919–15,938, doi:10.1029/94JB00852.
Jellinek, A. M., and M. Manga (2002), The influence of a chemical boundary layer on the fixity, spacing and lifetime of mantle plumes, *Nature*, *418*(6899), 760–763.
Karato, S.-i., and P. Wu (1993), Rheology of the upper mantle: A synthesis, *Science*, *260*(5109), 771–778.
Labrosse, S. (2002), Hotspots, mantle plumes and core heat loss, *Earth Planet. Sci. Lett.*, *199*(1), 147–156.
Leng, W., and M. Gurnis (2012), Shape of thermal plumes in a compressible mantle with depth-dependent viscosity, *Geophys. Res. Lett.*, *39*, L05310, doi:10.1029/2012GL050959.
Leng, W., and S. Zhong (2008), Controls on plume heat flux and plume excess temperature, *J. Geophys. Res*, *113*, B04408, doi:10.1029/2007JB005155.
Lloyd, S. (1982), Least squares quantization in PCM, *IEEE Trans. Inf. Theory*, *28*(2), 129–137.
Masters, G., G. Laske, H. Bolton, and A. Dziewonski (2000), The relative behaviour of shear velocity, bulk sound speed, and compressional velocity in the mantle: Implications for chemical and thermal structure, in Earth's Deep Interior: Mineral Physics and Tomography from

the Atomic to the Global Scale, *Geophys. Monogr. Ser.*, edited by S. Karato, et al., vol. 117, pp. 63–87, AGU, Washington, D. C., doi: 10.1029/GM117.
McNamara, A. K., and S. Zhong (2004), Thermochemical structures within a spherical mantle: Superplumes or piles?, *J. Geophys. Res*, *109*, B07402, doi:10.1029/2003JB002847.
McNamara, A. K., and S. Zhong (2005), Thermochemical structures beneath Africa and the Pacific Ocean, *Nature*, *437*(7062), 1136–1139.
Montague, N. L., and L. H. Kellogg (2000), Numerical models of a dense layer at the base of the mantle and implications for the geodynamics of d, *J. Geophys. Res.*, *105*(B5), 11,101–11,114.
Morgan, W. J. (1971), Convection plumes in the lower mantle, *Nature*, *230*, p. 42–43.
Nakagawa, T., and P. J. Tackley (2005), The interaction between the post-perovskite phase change and a thermo-chemical boundary layer near the core–mantle boundary, *Earth Planet. Sci. Lett.*, *238*(1), 204–216.
Ni, S., E. Tan, M. Gurnis, and D. Helmberger (2002), Sharp sides to the African superplume, *Science*, *296*, 1850–1852, doi:10.1126/science.1070698.
Renka, R. J. (1984), Interpolation of data on the surface of a sphere, *ACM Trans. Math. Software*, *10*(4), 417–436.
Renka, R. J. (1997), Algorithm 773: SSRFPACK: Interpolation of scattered data on the surface of a sphere with a surface under tension, *ACM Trans. Math. Software*, *23*(3), 435–442.
Richards, M. A., B. H. Hager, and N. H. Sleep (1988), Dynamically supported geoid highs over hotspots: Observation and theory, *J. Geophys. Res*, *93*(B7), 7690–7708.
Richards, M. A., R. A. Duncan, and V. E. Courtillot (1989), Flood basalts and hot-spot tracks: Plume heads and tails, *Science*, *246*(4926), 103–107.
Samuel, H., and C. G. Farnetani (2003), Thermochemical convection and helium concentrations in mantle plumes, *Earth Planet. Sci. Lett.*, *207*(1), 39–56.
Schilling, J.-G. (1991), Fluxes and excess temperatures of mantle plumes inferred from their interaction with migrating mid-ocean ridges, *Nature*, *352*, 397–403.
Seton, M., et al. (2012), Global continental and ocean basin reconstructions since 200 Ma, *Earth Sci. Rev.*, *113*(3), 212–270.
Sleep, N. H. (1988), Gradual entrainment of a chemical layer at the base of the mantle by overlying convection, *Geophys. J. Int.*, *95*(3), 437–447.
Sleep, N. H. (1990), Hotspots and mantle plumes: Some phenomenology, *J. Geophys. Res.*, *95*(B5), 6715–6736.
Sleep, N. H. (2006), Mantle plumes from top to bottom, *Earth Sci. Rev.*, *77*(4), 231–271.
Solheim, L. P., and W. R. Peltier (1990), Heat transfer and the onset of chaos in a spherical, axisymmetric, anelastic model of whole mantle convection, *Geophys. Astrophys. Fluid Dyn.*, *53*(4), 205–255, doi:10.1080/03091929008208928.
Squillacote, A. H., and J. Ahrens (2007), *The Paraview Guide*, vol. 230, pp. 42–43, Kitware.
Steinberger, B. (2000), Plumes in a convecting mantle: Models and observations for individual hotspots, *J. Geophys. Res.*, *105*(B5), 11,127–11,152.
Steinberger, B., and M. Antretter (2006), Conduit diameter and buoyant rising speed of mantle plumes: Implications for the motion of hot spots and shape of plume conduits, *Geochem. Geophys. Geosyst.*, *7*, Q11018, doi:10.1029/2006GC001409.
Steinberger, B., and A. R. Calderwood (2006), Models of large-scale viscous flow in the earth's mantle with constraints from mineral physics and surface observations, *Geophys. J. Int.*, *167*(3), 1461–1481, doi:10.1111/j.1365-246X.2006.03131.x.
Steinberger, B., and T. H. Torsvik (2008), Absolute plate motions and true polar wander in the absence of hotspot tracks, *Nature*, *452*(7187), 620–623.
Steinberger, B., and T. H. Torsvik (2012), A geodynamic model of plumes from the margins of large low shear velocity provinces, *Geochem. Geophys. Geosyst.*, *13*, Q01W09, doi:10.1029/2011GC003808.
Su, W.-j., and A. M. Dziewonski (1997), Simultaneous inversion for 3-D variations in shear and bulk velocity in the mantle, *Phys. Earth Planet. Inter.*, *100*(1), 135–156.
Tackley, P. J. (1996), Effects of strongly variable viscosity on three-dimensional compressible convection in planetary mantles, *J. Geophys. Res.*, *101*(B2), 3311–3332.
Tackley, P. J. (1998), Three-dimensional simulations of mantle convection with a thermo-chemical basal boundary layer: D'?, in The Core-Mantle Boundary Region, edited by M. Gurnis, et al., vol. 28, pp. 231–254, AGU, Washington, D. C., doi:10.1029/GD028.
Tackley, P. J. (2012), Dynamics and evolution of the deep mantle resulting from thermal, chemical, phase and melting effects, *Earth Sci. Rev.*, *110*(1), 1–25.
Tackley, P. J., and S. D. King (2003), Testing the tracer ratio method for modeling active compositional fields in mantle convection simulations, *Geochem. Geophys. Geosyst. 4*(4), 8302, doi:10.1029/2001GC000214.
Tan, E., and M. Gurnis (2005), Metastable superplumes and mantle compressibility, *Geophys. Res. Lett.*, *32*, L20307, doi:10.1029/2005GL024190.
Tan, E., W. Leng, S. Zhong, and M. Gurnis (2011), On the location of plumes and lateral movement of thermochemical structures with high bulk modulus in the 3-D compressible mantle, *Geochem. Geophys. Geosyst. 12*, Q07005, doi:10.1029/2011GC003665.
Torsvik, T. H., M. A. Smethurst, K. Burke, and B. Steinberger (2006), Large igneous provinces generated from the margins of the large low-velocity provinces in the deep mantle, *Geophys. J. Int.*, *167*(3), 1447–1460.
Torsvik, T. H., B. Steinberger, L. R. M. Cocks, and K. Burke (2008), Longitude: linking earth's ancient surface to its deep interior, *Earth Planet. Sci. Lett.*, *276*(3), 273–282.
Tosi, N., D. A. Yuen, N. de Koker, and R. M. Wentzcovitch (2013), Mantle dynamics with pressure- and temperature-dependent thermal expansivity and conductivity, *Phys. Earth Planet. Inter.*, *217*(0), 48–58, doi:10.1016/j.pepi.2013.02.004.
Van der Meer, D. G., W. Spakman, D. J. van Hinsbergen, M. L. Amaru, and T. H. Torsvik (2009), Towards absolute plate motions constrained by lower-mantle slab remnants, *Nat. Geosci.*, *3*(1), 36–40.
Zhang, N., S. Zhong, W. Leng, and Z.-X. Li (2010), A model for the evolution of the earth's mantle structure since the early paleozoic, *J. Geophys. Res*, *115*, B06401, doi:10.1029/2009JB006896.
Zhong, S. (2005), Dynamics of thermal plumes in three-dimensional isoviscous thermal convection, *Geophys. J. Int.*, *162*(1), 289–300.
Zhong, S. (2006), Constraints on thermochemical convection of the mantle from plume heat flux, plume excess temperature, and upper mantle temperature, *J. Geophys. Res.*, *111*, B04409, doi:10.1029/2005JB003972.
Zhong, S., and B. H. Hager (2003), Entrainment of a dense layer by thermal plumes, *Geophys. J. Int.*, *154*(3), 666–676.
Zhong, S., M. T. Zuber, L. Moresi, and M. Gurnis (2000), Role of temperature-dependent viscosity and surface plates in spherical shell models of mantle convection, *J. Geophys. Res.*, *105*(B5), 11,063–11,082, doi:10.1029/2000JB900003.
Zhong, S., A. McNamara, E. Tan, L. Moresi, and M. Gurnis (2008), A benchmark study on mantle convection in a 3-D spherical shell using citcoms, *Geochem. Geophys. Geosyst.*, *9*, Q10017, doi:10.1029/2008GC002048.